applied sciences

MDPI

Article

A Novel Constant Power Factor Loop for Stable *V/f* Control of PMSM in Comparison against Sensorless FOC with Luenberger-Type Back-EMF Observer Verified by Experiments

Michal Vidlak [1,*], Pavol Makys [1] and Lukas Gorel [2]

[1] Department of Power Systems and Electric Drives, Faculty of Electrical Engineering and Information Technology, University of Zilina, Univerzitna 1, 010 26 Zilina, Slovakia
[2] Vehicle Control & Networking Solutions, NXP Semiconductors, 1. Maje 1009, 756 61 Roznov pod Radhostem, Czech Republic
* Correspondence: michal.vidlak@feit.uniza.sk

Abstract: This paper proposes a novel constant power factor loop in the V/f control strategy with stabilization for a permanent magnet synchronous motor (PMSM). The advantage of such an algorithm is the independence of the machine parameters, which vary under different operational conditions, e.g., with temperature, magnetic core saturation, and skin-effect. Furthermore, it is a low-cost and simple-to-implement sensorless solution. The proposed strategy is compared against traditional sensorless FOC with a Luenberger-type back-electromotive force (EMF) observer, which can be designed based on the machine model. The output of this kind of observer is typically an error signal, which can be specified for position deviation, requiring phase-locked loop (PLL) algorithm implementation. Employing PLL, a rotor speed and position can be estimated from such an error. Therefore, it is a complex sensorless technique with high-performance microcontroller unit (MCU) requirements. Both strategies are deeply analyzed, mathematically described, and compared within the paper. At the end of the paper, these sensorless strategies are supported by experimental verification with a traction PMSM designed for golf cart applications, and the pros and cons of both techniques are discussed.

Keywords: sensorless control; Luenberger-type back-EMF observer; V/f control; power factor control; permanent magnet synchronous motor

Citation: Vidlak, M.; Makys, P.; Gorel, L. A Novel Constant Power Factor Loop for Stable V/f Control of PMSM in Comparison against Sensorless FOC with Luenberger-Type Back-EMF Observer Verified by Experiments. *Appl. Sci.* **2022**, *12*, 9179. https://doi.org/10.3390/app12189179

Academic Editors: Javier Poza, Gaizka Ugalde and Gaizka Almandoz

Received: 20 August 2022
Accepted: 12 September 2022
Published: 13 September 2022

1. Introduction

The sensorless techniques for different types of electric machines are still improving, especially in the automotive industry. PMSMs are highly demanded in such applications for their high power density factor, high dynamic features, robustness, and high efficiency. Due to cost reduction, which is a critical factor, especially in the automotive industry, researchers are forced to find new solutions for not only electrical drive but also the battery management system, power electronics, machine design, or software modifications of different control strategies. In particular, sensorless strategies are still very popular and attractive, because they offer the elimination of mechanical speed or position sensors coupled with the rotor shaft. This eliminates potential troubles coming mainly from the mechanical connection but also coming with vibration or temperature instability. A damaged sensor or one with inappropriate functionality would completely disable further motor operation in a sensored motor drive. Therefore, a proper sensorless algorithm could improve the minimization of the final cost, and furthermore, this solution decreases drive volume or maintenance cost. However, sensorless control could also offer a specified level of redundancy in case of a sudden mechanical sensor failure, which could be even more attractive, especially in the automotive industry but not only in this field. In general, sensorless vector control is one of the alternatives for operating PMSM without a mechanical sensor. The second alternative is a simpler scalar control, which also offers some benefits.

Vector control provides separate torque and flux control in AC machines. Such a control strategy is similar to separately excited DC machines, in which a mechanical commutator maintains such effect. Field-oriented control (FOC) is a common form of vector control. This control strategy is primarily used for applications requiring high dynamic performance, such as servo systems. In FOC, the control reference frame is oriented on the flux vector. Therefore, the position of the flux vector has to be identified to ensure precise and reliable speed or position control. The most accurate way to determine its position is through the mechanical sensor. The other way to distinguish the location of the flux vector is estimating its position by employing a sensorless algorithm. In this case, the requirement of a mechanical sensor is eliminated. The sensorless algorithms could be divided into two basic groups: model-based (back-EMF-based) and non-model based methods (well known as saliency-based methods).

The model-based methods, as the name says, include an exact mathematical model consisting of differential equations. The main idea is to estimate the back-EMF from stator voltages and currents and then use this information to estimate rotor position and speed. These methods provide a satisfactory control performance in medium- and high-speed regions, and many algorithms have been proposed. These include an extended Kalman filter (EKF) [1–3], a model reference adaptive system (MRAS) [4], a Luenberger observer [5], and a sliding mode observer (SMO) [6–11]. There are also other methods such as a least-order observer [12] and a disturbance observer [13]. These two employ an extended EMF term and can be applied for interior PMSM (IPMSM), where the rotor position information is contained not only in the flux or the EMF but also in the inductances due to their saliency. In [14,15], authors used a special asymptotic state observer with PLL. A different approach is proposed in [16], where an adaptive observer has been used. As was mentioned above, the main drawback of model-based estimators is in low-speed regions, where they are not applicable for well-known reasons (mostly for an unfavorable signal-to-noise ratio of the voltage measurement). Different start-up algorithms have to be applied to overcome this problem [17–19]. Another question is parameter variation, especially the precision of current and voltage measurement, which influences the final quality of estimation. Many of these aspects can be compensated [20,21]. In [22], the inductance compensation method is presented to achieve enhanced torque control performance against parameter variation. The adverse effects of the inverter harmonics were minimized in [23,24] with voltage error compensation techniques. The low-speed limit evaluation of back-EMF tracking was discussed in [25].

The non-model-based strategies offer parameter sensitiveness and work effectively in zero and low-speed regions. However, these methods basically require any type of signal injection, high-frequency (HF) voltage [26–32], or HF current [33] injection to utilize the rotor saliency. Some methods can also be used for the surface PMSM (SPMSM), where the d and q axis of the rotor are geometrically symmetrical [30–32]. The HF voltage injection causes the saliency reflected current, including the rotor position information. Demodulation processes are then used depending on various voltage and current injection types to retrieve the rotor speed and position. Band-pass and low-pass filters are widely used to obtain a rotor position error signal in the demodulation process. However, these filters inevitably have drawbacks, such as a time delay of the rotor speed or position estimation and a limitation of current controllers' bandwidth [29]. Square-wave injection methods [34–37] are used to solve these issues. They offer an extended range of injected voltage frequency, and accordingly, the bandwidth of the current controllers can be significantly enhanced. As a result, dynamic control performance can be improved. However, there are some adverse effects of the signal injection methods, for example, increased losses, torque ripples, and acoustic noises. Furthermore, the maximum inverter output voltage at higher speeds could limit the additional injected signal. Consequently, it is recommended to use the magnetic saliency-based method with signal injection at a standstill and low-speed range and a back-EMF-based technique above a certain threshold speed in the medium- and high-speed region [38] to provide sensorless control of PMSM in a wide speed range.

In some papers, strategies also known as hybrid techniques have been proposed to provide a full-speed-range sensorless drive. They usually represent a combination of back-EMF-based and magnetic saliency-based techniques. In [39,40], a transition algorithm is proposed to achieve a smooth operation between the two estimation methods. Furthermore, the combination of the model-based dynamic feedforward control and current injection is proposed in [33].

In comparison with FOC, scalar control is simpler and could be an ideal low-cost alternative in some applications where high dynamic performance is not crucial, such as fans, compressor drives, or pumps. It is a strategy in which a motor terminal voltage V changes in proportion to the applied frequency f, and hence, it can also be expressed as V/f control. It maintains constant machine flux and thus constant torque production capability up to the rated machine speed. Using V/f control, a stator resistance voltage drop can be neglected at higher frequencies. However, the voltage drop cannot be ignored at lower frequencies. In this region, boost voltage can be applied to the machine to compensate for the voltage drop. This allows the motor to develop the necessary torque even at lower speeds [41]. The other disadvantage of scalar control is a possible loss of synchronism, leading to instability issues. For this purpose, a stabilizing loop may be applied to modulate reference frequency and thus maintain synchronism. This correction provides system damping and reduces the speed oscillations, stabilizing the system [42–44]. Some authors have presented different approaches to V/f control. In [44], stable V/f control with high-efficiency control is compared against sensorless FOC. Sensorless vector control in [44] is composed of two estimation algorithms. The first is the saliency-based method with HF frequency injection for low-speed operation. In the high-speed region, a back-EMF-based method is used. However, the employed algorithms are not further specified in the paper. V/f control including stabilizing loop is discussed in [43]. In [45], a high-efficiency V/f control loop used a single DC shunt current measurement. Other authors in [46,47] used different types of maximum torque per ampere (MTPA) methods based on imaginary power factor calculation suitable for a V/f controlled PMSM drive. The control V/f algorithms based on unity power factor (UPF) calculation are simulated and experimentally verified in [48,49]. A similar technique is applied and compared with FOC in [50,51], where active flux observer and MTPA are used. Stable V/f control with UPF was compared to back-EMF-based sensorless FOC in [52], supported by simulation analysis. In [53], the MTPA method, field-weakening, maximum torque per voltage (MTPV), and energy optimal V/f control are proposed. V/f control with MTPA for SPMSM based on HF voltage signal injection is presented in [54].

This paper proposes a novel constant power factor loop in the V/f control strategy with stabilization. The proposed V/f control does not require information about PMSM parameters and is robust against its variations. These parameters vary during motor operation, e.g., with the magnetic core saturation, temperature, and skin effect. Furthermore, the proposed V/f control structure does not require the direct calculation of phase shift between current and voltage, as employed in [48,49]. Instead, the phase shift can be controlled directly in the voltage vector reference frame $d_v q_v$ based on the demanded power factor. The proposed strategy is then compared to the traditional sensorless FOC with Luenberger-type back-EMF observer, which can be designed based on the machine model. Both strategies are deeply analyzed, mathematically described, and compared within the paper. At the end of the paper, these sensorless strategies are supported by experimental verification with the traction PMSM designed for golf cart applications, and the pros and cons of both techniques are discussed.

2. Mathematical Model of PMSM

The equations describing voltages in the three phase windings of PMSM can be written in matrix form. If symmetrical three-phase winding on the stator is supposed, then it can be assumed that their resistances are identical: $R_a = R_b = R_c = R_s$. In the mathematical model, the saturation and temperature effects are also neglected [55].

$$\begin{bmatrix} v_a \\ v_b \\ v_c \end{bmatrix} = R_s \begin{bmatrix} i_a \\ i_b \\ i_c \end{bmatrix} + \frac{d}{dt} \begin{bmatrix} \psi_a \\ \psi_b \\ \psi_c \end{bmatrix} \tag{1}$$

where v_a, v_b, v_c are the three phase stator voltages, R_s is the stator resistance, i_a, i_b, i_c are the three phase stator currents, and ψ_a, ψ_b, ψ_c are the three phase stator flux linkages, given as:

$$\begin{bmatrix} \psi_a \\ \psi_b \\ \psi_c \end{bmatrix} = \begin{bmatrix} L_{aa} & L_{ab} & L_{ac} \\ L_{ba} & L_{bb} & L_{bc} \\ L_{ca} & L_{cb} & L_{cc} \end{bmatrix} \begin{bmatrix} i_a \\ i_b \\ i_c \end{bmatrix} + \psi_{pm} \begin{bmatrix} \cos(\theta_e) \\ \cos(\theta_e - \frac{2\pi}{3}) \\ \cos(\theta_e + \frac{2\pi}{3}) \end{bmatrix} \tag{2}$$

where L_{aa}, L_{bb}, L_{cc} are stator phase self-inductances, $L_{ab} = L_{ba}$, $L_{bc} = L_{cb}$, $L_{ca} = L_{ac}$ are mutual inductances between respective stator phases, ψ_{pm} is the permanent magnet flux linkage, and θ_e is the electrical rotor position. By means of Clarke and Park transformation, three phase voltage (1) and flux equations (2) can be transformed to the rotational reference frame dq:

$$\begin{bmatrix} v_d \\ v_q \end{bmatrix} = R_s \begin{bmatrix} i_d \\ i_q \end{bmatrix} + \frac{d}{dt} \begin{bmatrix} \psi_d \\ \psi_q \end{bmatrix} + \omega_e \begin{bmatrix} -\psi_q \\ \psi_d \end{bmatrix} \tag{3}$$

where v_d and v_q are the dq axis voltages, i_d and i_q are the dq axis currents, ω_e is the electrical angular velocity, and ψ_d, ψ_q are the dq axis flux linkages, defined as:

$$\begin{bmatrix} \psi_d \\ \psi_q \end{bmatrix} = \begin{bmatrix} L_d & 0 \\ 0 & L_q \end{bmatrix} \begin{bmatrix} i_d \\ i_q \end{bmatrix} + \psi_{pm} \begin{bmatrix} 1 \\ 0 \end{bmatrix} \tag{4}$$

where L_d and L_q are the dq axis inductances. Substituting (4) into (5), the voltage equations of the PMSM in dq coordinates lead to the following form:

$$\begin{bmatrix} v_d \\ v_q \end{bmatrix} = R_s \begin{bmatrix} i_d \\ i_q \end{bmatrix} + \begin{bmatrix} L_d & 0 \\ 0 & L_q \end{bmatrix} \frac{d}{dt} \begin{bmatrix} i_d \\ i_q \end{bmatrix} + \omega_e \begin{bmatrix} -L_q \\ L_d \end{bmatrix} \begin{bmatrix} i_q \\ i_d \end{bmatrix} + \omega_e \psi_{pm} \begin{bmatrix} 0 \\ 1 \end{bmatrix} \tag{5}$$

The mathematical model of PMSM in rotational reference frame dq is very popular for FOC structures, because both controllable quantities, current and voltage, are DC values, as is evident from Figure 1. In addition, it allows employing simple controllers to force the machine currents to the required states.

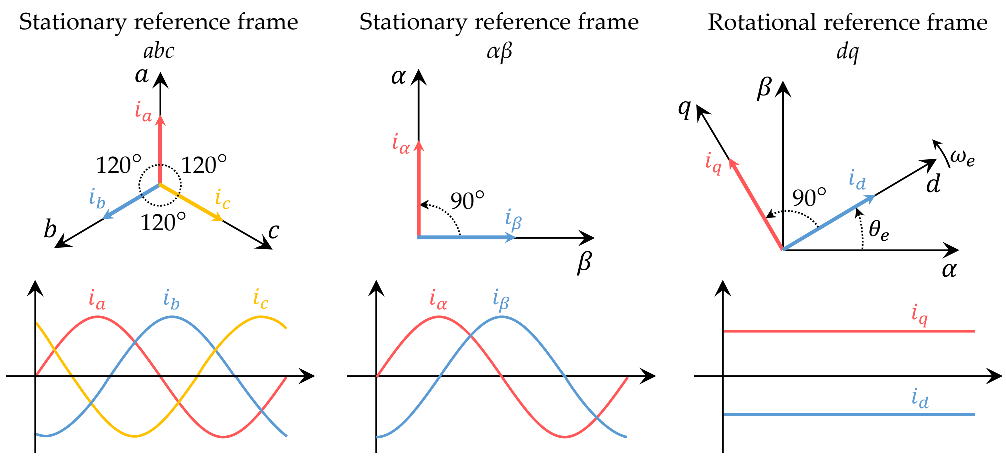

Figure 1. Transformation from stationary to rotational reference frame.

The other important quantity of the machine is the electromagnetic torque. The electromagnetic torque of the PMSM machine in rotational reference frame dq is defined as:

$$T_e = \frac{3}{2} p \left[\psi_{pm} i_q + (L_d - L_q) i_d i_q \right] \tag{6}$$

where p is the number of pole pairs. The first term in Equation (6) represents a synchronous torque produced by the permanent magnet flux, and the second term is a reluctance torque dependent on the rotor saliency. Both terms reflect an essential aspect of the torque production in the PMSM machine. By sublimation of electromagnetic torque and load torque, the mechanical equation of PMSM can be presented as:

$$T_e - T_L = J \frac{d\omega_m}{dt} \tag{7}$$

where T_L is the load torque, J is the moment of inertia, and ω_m is the mechanical angular velocity. The block diagram of the PMSM in rotational reference frame dq is illustrated in Figure 2 [55]:

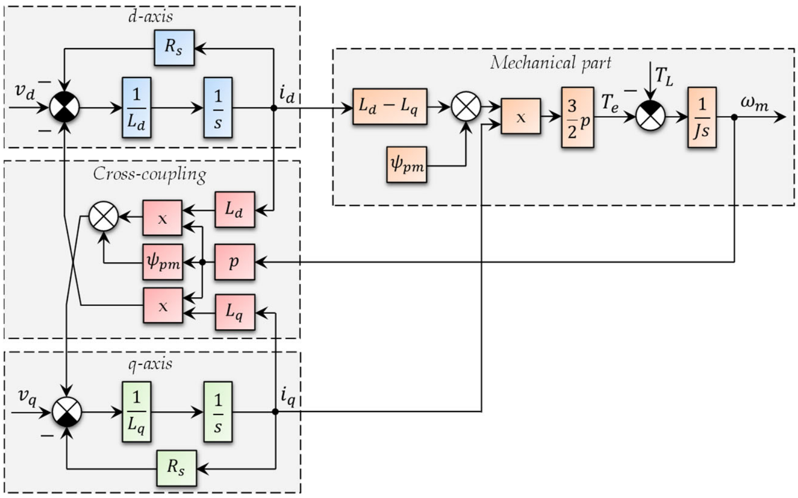

Figure 2. Block diagram of the PMSM in rotational reference frame dq.

3. Sensorless FOC with Luenberger-Type Back-EMF Observer

The back-EMF observer can be used in conjunction with the vector control strategy, as shown in Figure 3.

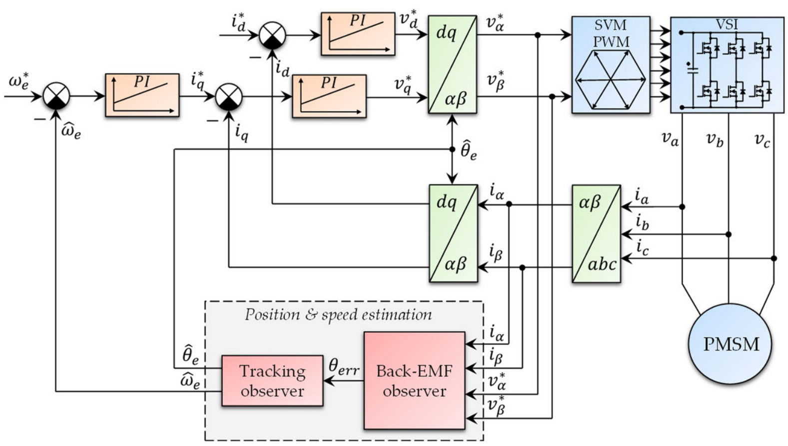

Figure 3. Block diagram of the sensorless FOC with the Luenberger-type back-EMF observer and tracking observer.

Such a scheme can provide an alternative or redundant solution to the sensored control drive. Thus, the drive is considered sensorless by removing the mechanical sensor from the rotor shaft and estimating rotor speed or position. However, this kind of observer does not provide direct feedback on rotor speed and position. To solve this issue, a tracking observer can be used to process the output of the back-EMF observer. However, this sensorless strategy is based on the machine model, and it is very complex, leading to higher computational requirements for MCU. Furthermore, the implementation and correct tuning of the several PI controllers, filters, etc., may be time-consuming. Table 1 shows the main functions employed in this sensorless structure.

Table 1. Sensorless FOC with the Luenberger-type back-EMF observer—complexity.

Control Structure	PI	I	Park	Clarke	Atan	Filters
Sensorless FOC with the Luenberger-type back-EMF observer	6	1	4	1	1	2

However, one should notice that the sensorless components in Table 1 are not matching with the block diagram in Figure 3 because the other components are part of the back-EMF observer and tracking observer blocks. These are illustrated within the next sections.

3.1. Sensorless FOC

FOC is a common form of vector control. It is a cascade control structure with an inner current and outer speed loop. The control loops placed in series represent feedback in a closed-loop system. However, a transformation of the controllable motor quantities, such as current and voltage, from the stationary *abc* to the rotational reference system *dq* must be conducted. In the *dq* coordinates, these variables become DC values. Thus, simple controllers can control such quantities, as shown in Figure 4.

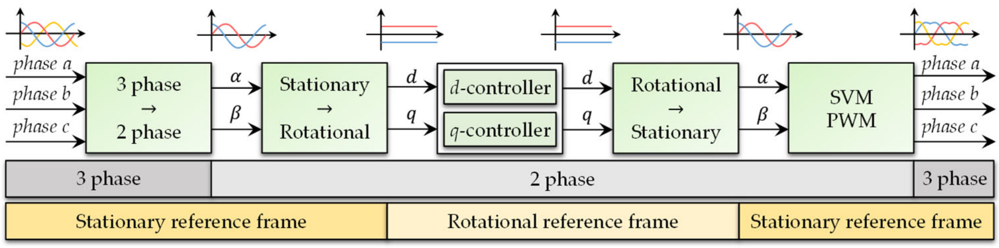

Figure 4. Transformations in FOC scheme.

PI controllers are commonly used to maintain demanded behavior by minimizing the error between required and feedback variables. The parameters of these controllers, more specifically proportional and integral gain, have to be correctly calculated to adjust the dynamics of the whole system.

3.1.1. Current Loop

FOC is based on independent control of the machine torque and flux. Generally, the torque-producing component is q-axis current, and the component responsible for machine flux production is d-axis current. These components are part of the inner current loop, with PI controllers placed for each path, as shown in Figure 3. By compensating the cross-coupling and back-EMF terms in (5), simplified voltage equations can be defined:

$$\begin{bmatrix} v_d \\ v_q \end{bmatrix} = R_s \begin{bmatrix} i_d \\ i_q \end{bmatrix} + \begin{bmatrix} L_d & 0 \\ 0 & L_q \end{bmatrix} \frac{d}{dt} \begin{bmatrix} i_d \\ i_q \end{bmatrix} \tag{8}$$

It is clear from (8) that the equations are identical in structure. Therefore, the same principle can be employed to calculate the gains of the controllers in both axes. The only difference lies in L_d and L_q, which leads to different proportional and integral gains K_P, K_I. To accurately describe the current control loop, the transfer functions of A/D converters and the voltage source inverter with a PWM modulator have to be evaluated. Moreover, the sampling time of the current loop and discrete form of the controllers have to be considered. However, the effects of A/D converter and inverter transportation delay are neglected to simplify the controller design. The closed-current loop can then be designed with the following transfer functions representing RL circuit and current controller:

$$F_{RL}(s) = \frac{1}{Ls + R_s} \tag{9}$$

$$F_{PI_i}(s) = \frac{K_{P_i}s + K_{I_i}}{s} \tag{10}$$

where K_{P_i}, K_{I_i} are the proportional and integral gains of the current controller. The transfer function of a simplified closed-current loop can be derived based on (9) and (10):

$$F_i(s) = \frac{F_{PI_i}(s)F_{RL}(s)}{1 + F_{PI_i}(s)F_{RL}(s)} = \frac{\frac{K_{P_i}}{L}s + \frac{K_{I_i}}{L}}{s^2 + \left(\frac{K_{P_i}+R_s}{L}\right)s + \frac{K_{I_i}}{L}} \tag{11}$$

The block diagram of the simplified current control loop with compensated cross-coupling and back-EMF terms is illustrated in Figure 5.

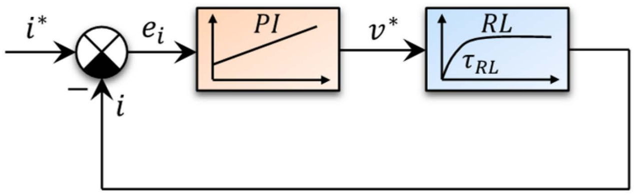

Figure 5. Block diagram of the simplified current loop scheme.

The characteristic Equation of (11) reveals a second-order system. However, the nominator of the transfer function introduces zero due to the PI controller. It increases the system overshoot, lowering the potential closed-loop bandwidth. The zero can be compensated by a zero-cancellation block in the feedforward. The zero-cancellation block can be considered as a first-order filter with the following transfer function:

$$F_{ZC_i}(s) = \frac{1}{\frac{K_{P_i}}{K_{I_i}}s + 1} \tag{12}$$

Introducing (12) to (11), the closed-current loop transfer function will be rearranged as:

$$F_i(s) = \frac{F_{PI_i}(s)F_{RL}(s)}{1 + F_{PI_i}(s)F_{RL}(s)} = \frac{\frac{K_{I_i}}{L}}{s^2 + \left(\frac{K_{P_i}+R_s}{L}\right)s + \frac{K_{I_i}}{L}} \tag{13}$$

The block diagram of the simplified closed-current loop with zero-cancellation is presented in Figure 6.

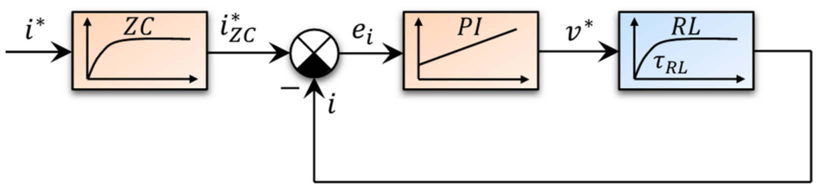

Figure 6. Block diagram of the simplified current loop scheme with zero-cancellation.

Finally, the proportional and integral gains of the current controller can be designed by comparing the closed-loop characteristic polynomial with the ideal second-order system:

$$s^2 + \left(\frac{K_{P_i} + R_s}{L}\right)s + \frac{K_{I_i}}{L} = s^2 + 2\xi_i \omega_{0_i} s + \omega_{0_i}^2 \tag{14}$$

where ω_{0_i} is the natural frequency of the current loop, and ξ_i is the damping factor of the current loop. The proportional and integral gains of the current controller in continuous domain can be then derived from (14) as follows:

$$\begin{aligned} K_{P_i} &= 2\xi_i \omega_{0_i} L - R_s \\ K_{I_i} &= \omega_{0_i}^2 L \end{aligned} \tag{15}$$

However, the control loop is updated in discrete steps in real applications. Therefore, a discrete representation of the current controller has to be used:

$$\begin{aligned} K_{P_i}(z) &= K_{P_i} \\ K_{I_i}(z) &= K_{I_i} T_{s_i} \end{aligned} \tag{16}$$

where T_{s_i} is the sampling period of the current loop.

3.1.2. Speed Loop

The speed loop is the outer loop in the cascade control structure of FOC. In the speed loop, a PI controller is employed to provide appropriate speed control of the PMSM machine. The output of the speed controller creates a reference value for the q-axis current controller, as is evident in Figure 7. In most applications, it is advantageous to use a PI controller with an anti-windup function limiting the controller output and preventing current overload of the machine or inverter.

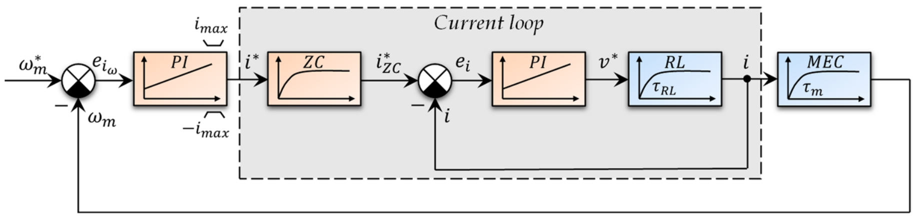

Figure 7. Block diagram of the speed loop.

An electrical time constant of the machine is usually much smaller than the time constant of the mechanical part. A small electrical time constant requires a higher sampling frequency of the current loop, while the speed loop operates at a lower sampling frequency. This ensures enough time to control the machine current between two speed samples properly. Therefore, the current loop can be considered the gain equal to 1. Furthermore, it simplifies the speed controller design, reducing the speed loop transfer function to a second-order system. The block diagram of the simplified speed loop scheme is presented in Figure 8.

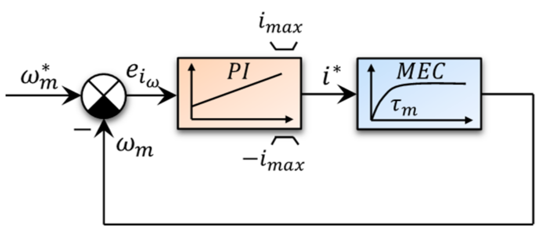

Figure 8. Block diagram of the simplified speed loop.

The closed speed loop can then be designed with the following transfer functions representing mechanical system and speed controller:

$$F_m(s) = \frac{k_T}{Js + B} \tag{17}$$

$$F_{PI_\omega}(s) = \frac{K_{P_\omega} s + K_{I_\omega}}{s} \tag{18}$$

where k_T is the torque constant, B is the viscous friction coefficient, and K_{P_ω}, K_{I_ω} are the proportional and integral gains of the speed controller. The transfer function of the speed loop can be created based on (17) and (18):

$$F_\omega(s) = \frac{F_{PI_\omega}(s)F_m(s)}{1 + F_{PI_\omega}(s)F_m(s)} = \frac{\frac{k_T K_{P_\omega}}{J}s + \frac{k_T K_{I_\omega}}{J}}{s^2 + \left(\frac{k_T K_{P_\omega} + B}{J}\right)s + \frac{k_T K_{I_\omega}}{J}} \tag{19}$$

Similarly, as in the current loop, zero is introduced in the nominator of (19) due to the PI controller increasing system overshoot. The zero can be compensated again with the zero-cancellation block, as shown in Figure 9, to improve the speed loop control performance during machine transients. As an alternative to the zero-cancellation block, a ramp function is commonly used in several applications to prevent system overshoot.

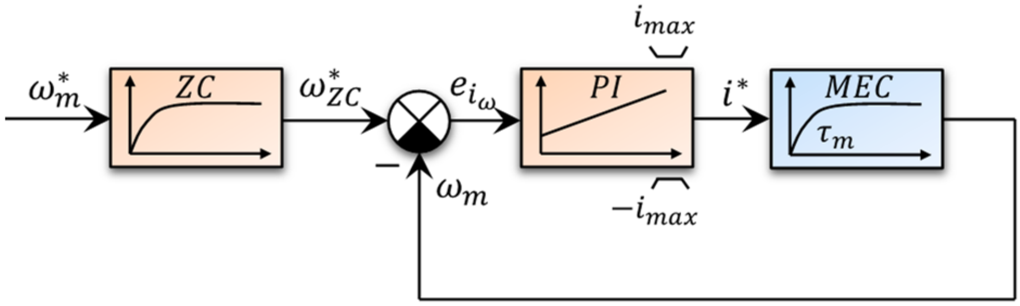

Figure 9. Block diagram of the simplified speed loop with zero-cancellation.

The transfer function of the zero-cancellation with speed controller gains is defined as:

$$F_{ZC_\omega}(s) = \frac{1}{\frac{K_{P_\omega}}{K_{I_\omega}}s + 1} \tag{20}$$

Introducing (20) into (19), the transfer function of the speed loop with compensated zero is in the following form:

$$F_\omega(s) = \frac{F_{PI_\omega}(s)F_m(s)}{1 + F_{PI_\omega}(s)F_m(s)} = \frac{\frac{k_T K_{I_\omega}}{J}}{s^2 + \left(\frac{k_T K_{P_\omega} + B}{J}\right)s + \frac{k_T K_{I_\omega}}{J}} \tag{21}$$

Comparing the characteristic polynomial of (21) with the ideal second-order system, the parameters of the speed controller can be derived as:

$$\begin{aligned} K_{P_\omega} &= \frac{2\xi_\omega \omega_{0_\omega} J - B}{k_T} \\ K_{I_\omega} &= \frac{J}{k_T}\omega_{0_\omega}^2 \end{aligned} \tag{22}$$

where ω_{0_ω} is the natural frequency of the speed loop, and ξ_ω is the damping factor of the speed loop. The discrete form of speed controller gains can be designed as:

$$
\begin{aligned}
K_{P_\omega}(z) &= K_{P_\omega} \\
K_{I_\omega}(z) &= K_{I_\omega} T_{s_\omega}
\end{aligned}
\tag{23}
$$

where T_{s_ω} is the sampling period of the speed loop.

It should be noticed that the current loop is usually maintained faster than the speed loop. The reason is that the electrical time constant of the motor is much smaller than the mechanical time constant of the motor, and so the small electrical time constant requires the current control loop to run at a higher sampling frequency. On the contrary, the speed loop can run in a slower control loop with a lower sampling frequency. This means that the natural frequency of the current loop will be always higher than the natural frequency of the speed loop. Such an approach provides enough time to control the current between two speed samples [56]. Furthermore, the damping factor can be maintained to influence the controller gains and dynamics response. The damping factor could be set at less than one (underdamped system), greater than one (overdamped system), or equal to one (critically damped system). For the second-order systems, the damping factor is usually set up to 0.707, to provide a system attenuation -3 dB at the controller cutoff frequency.

3.2. Luenberger-Type Back-EMF Observer

The primary purpose of this sensorless approach is to estimate the back-EMF voltage, which contains information about the rotor position. It is a method based on the mathematical model of the PMSM machine. Therefore, the mathematical model introduced in Section 1 is mandatory to describe this sensorless approach. The voltage equations of the PMSM in rotational reference frame dq depicted by (5) can be rearranged to the following form:

$$
\begin{bmatrix} v_d \\ v_q \end{bmatrix} = \begin{bmatrix} R_s + L_d s & -\omega_e L_q \\ \omega_e L_d & R_s + L_q s \end{bmatrix} \begin{bmatrix} i_d \\ i_q \end{bmatrix} + \omega_e \psi_{pm} \begin{bmatrix} 0 \\ 1 \end{bmatrix}
\tag{24}
$$

where s is the Laplace operator. However, (24) cannot be applied for a sensorless control, because the motor position is unavailable, and thus, the back-EMF voltage cannot be observed. Therefore, it is necessary to employ a new estimated rotational reference frame $\gamma\delta$ lagging from the origin dq rotational reference frame by an estimation position error θ_{err}, evident from Figure 10.

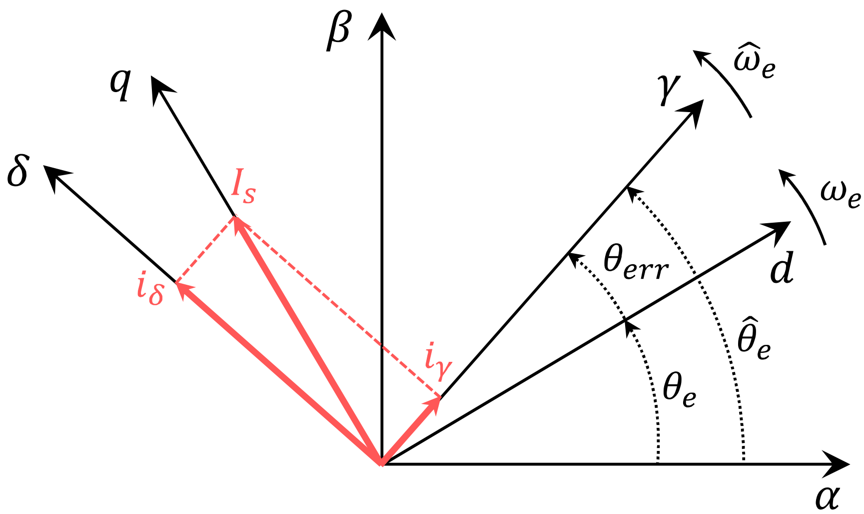

Figure 10. Vector diagram of PMSM defining stationary and rotating reference frames.

However, (24) has to be rewritten to the form with the symmetrical impedance matrix, as follows:

$$\begin{bmatrix} v_d \\ v_q \end{bmatrix} = \begin{bmatrix} R_s + L_d s & -\omega_e L_q \\ \omega_e L_q & R_s + L_d s \end{bmatrix} \begin{bmatrix} i_d \\ i_q \end{bmatrix} + E_{ex} \begin{bmatrix} 0 \\ 1 \end{bmatrix} \tag{25}$$

where E_{ex} is the extended EMF (EEMF) term equal to:

$$E_{ex} = \omega_e \left[\left(L_d - L_q \right) i_d + \psi_{pm} \right] - \left(L_d - L_q \right) s i_q \tag{26}$$

Afterward, (25) can be transformed to the estimated reference frame $\gamma\delta$, yielding voltage equations:

$$\begin{bmatrix} v_\gamma \\ v_\delta \end{bmatrix} = \begin{bmatrix} R_s + L_d s & -\omega_e L_q \\ \omega_e L_q & R_s + L_d s \end{bmatrix} \begin{bmatrix} i_\gamma \\ i_\delta \end{bmatrix} + \begin{bmatrix} e_\gamma \\ e_\delta \end{bmatrix} \tag{27}$$

where e_γ, e_δ are the $\gamma\delta$ components of EEMF:

$$\begin{bmatrix} e_\gamma \\ e_\delta \end{bmatrix} = E_{ex} \begin{bmatrix} -\sin(\theta_{err}) \\ \cos(\theta_{err}) \end{bmatrix} + (\hat{\omega}_e - \omega_e) L_d \begin{bmatrix} -i_\delta \\ i_\gamma \end{bmatrix} \tag{28}$$

where $\hat{\omega}_e$ is the estimated rotor speed. Assuming that error between the estimated speed $\hat{\omega}_e$ and actual rotor speed ω_e under steady-state condition is zero, the second part of (28) can be neglected. Afterward, the estimated $\gamma\delta$ components of EEMF become:

$$\begin{bmatrix} \hat{e}_\gamma \\ \hat{e}_\delta \end{bmatrix} = E_{ex} \begin{bmatrix} -\sin(\theta_{err}) \\ \cos(\theta_{err}) \end{bmatrix} \tag{29}$$

containing estimated position error θ_{err}. This variable can be extracted from (29) by employing arctan function as follows [12]:

$$\theta_{err} = \tan^{-1}\left(\frac{-\hat{e}_\gamma}{\hat{e}_\delta} \right) \tag{30}$$

This also reduces the effect of the back-EMF observer parameter variation. For example, if the d-axis inductance L_d is not accurate, it will affect the dynamic performance of the observer. On the other hand, stator resistance R_s will not influence the control dynamics. Instead, it will directly affect the resulting amplitude of the estimated back-EMF. However, the effects of the unprecise L_d, R_s are the same in both γ and δ axis, because the controller and observer models are identical in these axes. Therefore, by performing the division of EEMF $\gamma\delta$ components as in (30), the effects of the inaccurate L_d, R_s are compensated. Nevertheless, the q-axis inductance L_q is not compensated with such division, because the change in one axis is not proportional to the other one. This proves that such an observer is dependent on the machine parameters, where the uncertainty in L_q affects the steady-state accuracy of the observer. The block diagram of the back-EMF observer in the estimated rotational reference frame $\gamma\delta$ is presented in Figure 11.

It is evident in Figure 11 that the block diagram contains two PI controllers. The parameters of these controllers have to be properly calculated to allow correct control performance of the whole structure. Neglecting cross-coupling terms, the γ-axis and δ-axis loops are identical to the current loop structure discussed in Section 3.1.1. This means that the same principle can be used to calculate the proportional and integral gains of the back-EMF controller with respect to d-axis inductance:

$$\begin{aligned} K_{P_b} &= 2\xi_b \omega_{0_b} L_d - R_s \\ K_{I_b} &= \omega_{0_b}^2 L_d \end{aligned} \tag{31}$$

where ω_{0_b} is the natural frequency of the back-EMF observer, and ξ_b is the damping factor of the back-EMF observer. The natural frequency of the back-EMF observer is usually set close to the current loop bandwidth, while the damping factor is in intervals of approximately 0.5–1.5. The lower damping factors lead to higher overshoot but faster response and vice versa.

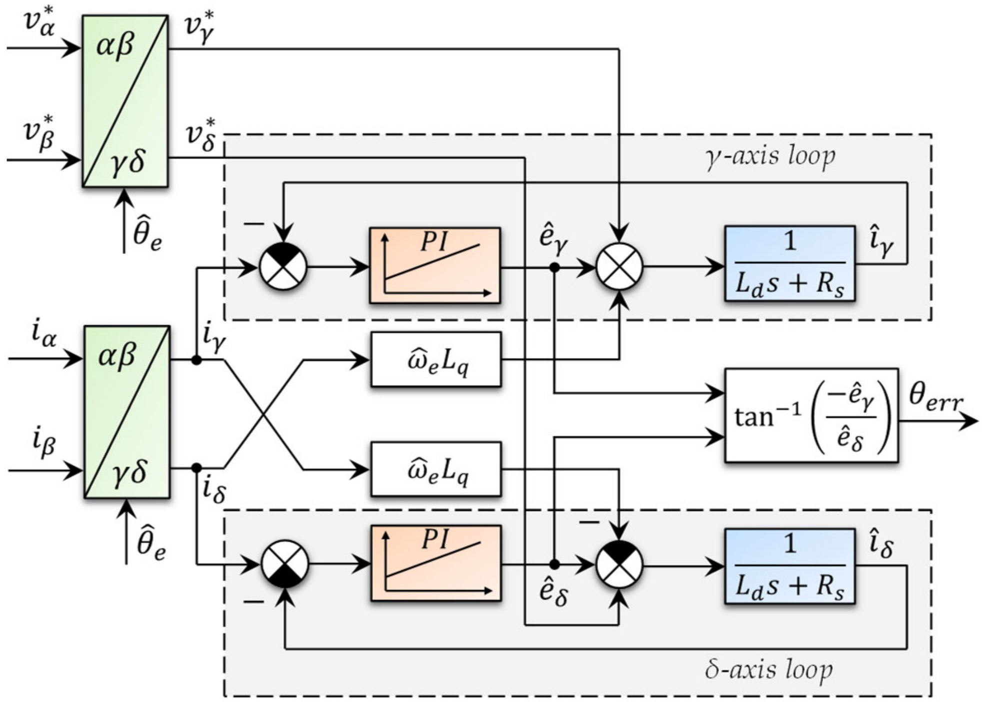

Figure 11. Luenberger-type back-EMF observer in the estimated rotating reference frame $\gamma\delta$.

3.3. Tracking Observer

The tracking observer is an essential part of sensorless FOC with a back-EMF observer. Since the output of the observer has an estimation position error θ_{err}, it is necessary to employ a structure that can force such error to zero ($\theta_{err} = 0$). The PLL can satisfy this requirement and thus provide zero displacements between the dq and estimated $\gamma\delta$ reference frame. The output of PLL is the estimated speed $\hat{\omega}_e$ and the estimated position $\hat{\theta}_e$. The PLL allows estimating the rotor speed without an undesirable position derivative. The estimated speed is used as a feedback value for the speed loop and to calculate cross-coupling terms, while the estimated position is employed as an angle to transform the voltages and currents from dq to the estimated $\gamma\delta$ reference frame. The block diagram of the back-EMF and tracking observer with the PLL mechanism is shown in Figure 12.

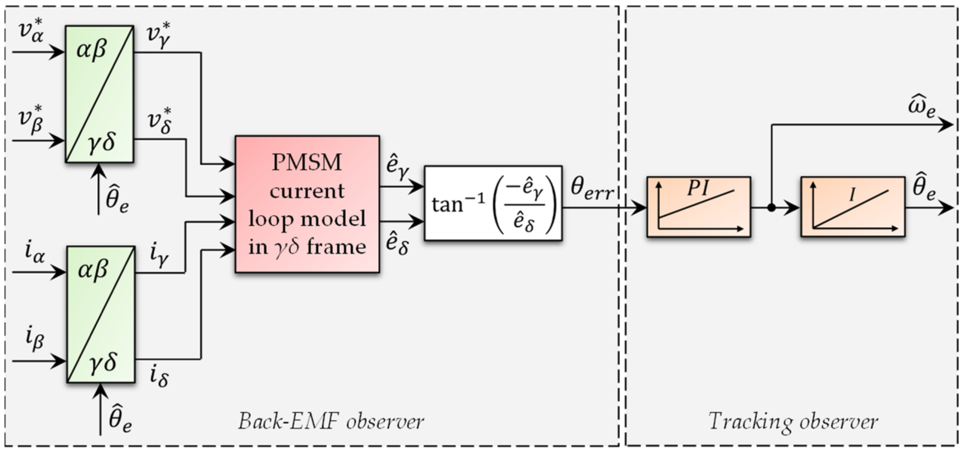

Figure 12. Back-EMF and tracking observer with PLL mechanism.

However, the tracking observer contains the PI controller, whose parameters have to be correctly calculated. They can be calculated from the linearized version of the observer shown in Figure 13.

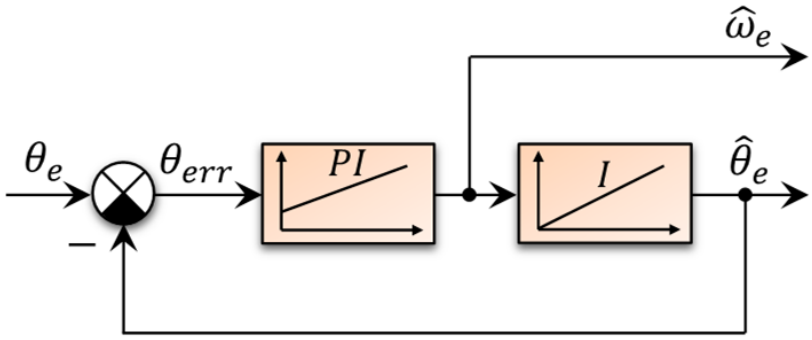

Figure 13. Linearized version of the tracking observer with PLL mechanism.

Similarly, the parameters can be calculated with the pole-placement method, yielding the following proportional and integral gains of the PLL controller [57]:

$$\begin{aligned} K_{P_{to}} &= 2\xi_{to}\omega_{0_{to}} \\ K_{I_{to}} &= \omega_{0_{to}}^2 \end{aligned} \tag{32}$$

4. Stable *V*/*f* Control with Constant Power Factor Loop

V/f control is a form of scalar control maintaining a constant ratio between stator voltage and required stator frequency. It is a good alternative in applications where highly dynamic control performance is not required, such as heating, ventilation, and air conditioning (HVAC), fans, or pumps. The V/f ratio is usually calculated from the nominal values of the PMSM. It provides an opportunity to control the PMSM machine without the mechanical sensor on the rotor shaft. The position sensor is not demanded, because the required $\alpha\beta$ voltages are calculated with a transformation angle obtained by integrating the required speed.

By employing the $V/$f control, the high-performance MCU needed in the FOC scheme is not required. It is a very simple control strategy composed of fewer functions than sensorless FOC, as evident from Table 2. For example, a single PI controller in V/f control instead of six in sensorless FOC avoids the time-consuming controller gains calculation. The sensorless components in the stabilizing and CPF loop are illustrated in the next sections. However, coming with this simplicity, there are also some drawbacks such as:

- Instability of the system after exceeding a specific applied frequency;
- Low dynamic performance;
- Poor fault protection against stall detection and overcurrent.

Table 2. Stable V/f control with constant power factor loop–complexity.

Control Structure	PI	I	Park	Clarke	Atan	Filters
Stable V/f control with constant power factor loop	1	1	2	1	0	1

Nevertheless, the first issue can be solved by employing the stabilizing loop to prevent undesired rotor oscillations. The second disadvantage may not be a problem in several applications, where high dynamic performance is not required.

The block diagram of the V/f control with stabilization and constant power factor loop is shown in Figure 14.

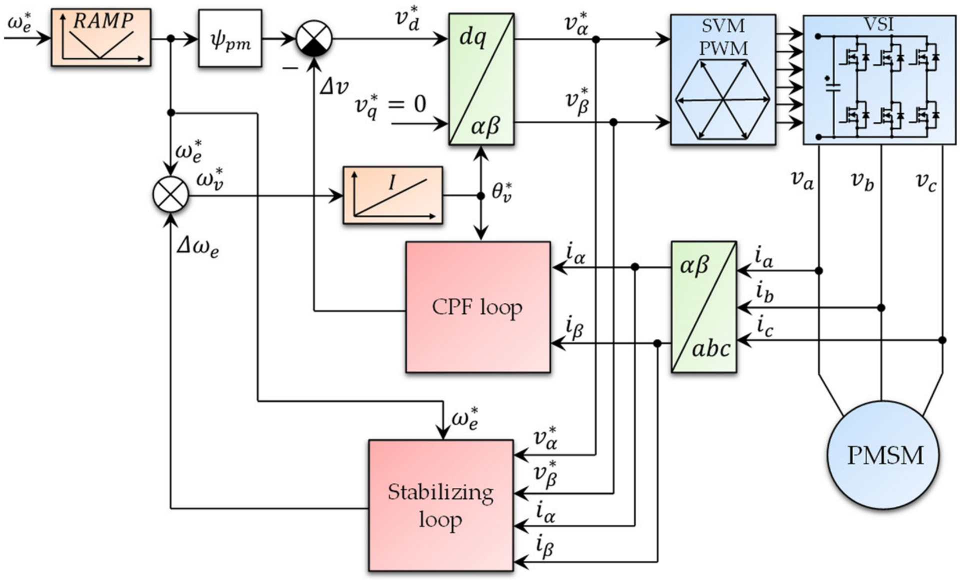

Figure 14. Block diagram of the stable V/f control with constant power factor loop.

4.1. Stabilizing Loop

The stabilizing loop can be implemented in the V/f control to prevent rotor oscillations, thus stabilizing the system. The principle of the stabilizing loop lies in the superimposition of the small frequency signal onto the required electrical angular velocity. The superimposed frequency signal must be of opposite polarity to the experienced perturbation. The perturbation can be extracted, for example, from:

- DC link current;
- Actual rotor speed;
- Input active power.

Each of the components requires some extra features to be employed or implemented. For the perturbation extraction from DC link current, a current sensor in DC bus is necessary, leading to higher additional costs. The extraction from the actual rotor speed can be considered as the most reliable. However, a position sensor is required for this purpose, removing advantages associated with sensorless control. The most practical with respect to the final cost is the solution that uses an input active power component. This strategy requires phase currents measurements, which is the common feature in the motor control drives. The transformation of the three phase currents from *abc* to $\alpha\beta$ reference frame must be performed to calculate the active power P_e as:

$$P_e = \frac{3}{2}\left(v_\alpha^* i_\alpha + v_\beta^* i_\beta\right) \tag{33}$$

where v_α^*, v_β^* are the required $\alpha\beta$ voltages and i_α, i_β are the measured $\alpha\beta$ currents. The input active power perturbation component ΔP_e can be extracted from origin signal with a first-order high-pass filter. It eliminates a DC component from the active power P_e, and the useful signal contains only higher-frequency components:

$$\Delta P_e = \frac{s}{s + \frac{1}{\tau_H}} P_e \tag{34}$$

where τ_H is the time constant of the high-pass filter. This constant can be experimentally determined regarding the speed oscillations [49]. Afterward, it is necessary to amplify the AC component of active power with proportional gain of the stabilizing loop K_S:

$$K_s = \frac{C_1}{\omega_e^*}, \omega_e^* \neq 0 \tag{35}$$

where C_1 is the stabilizing loop constant, which must be divided by the reference electrical angular velocity ω_e^* in order to maintain almost constant damping, particularly at higher frequencies. Then, the output of the stabilizing loop is the speed perturbation component $\Delta\omega_e$, which is superimposed onto the required velocity ω_e^* to stabilize scalar control:

$$\begin{aligned} \Delta\omega_e &= -K_s \Delta P_e \\ \omega_v^* &= \omega_e^* + \Delta\omega_e \end{aligned} \tag{36}$$

where ω_v^* is the voltage vector reference angular velocity. Integrating this variable, the voltage vector position θ_v^* is generated to perform Park transformation in feedforward path and constant power factor loop. The block diagram of the stabilizing loop is presented in Figure 15 [42,43]:

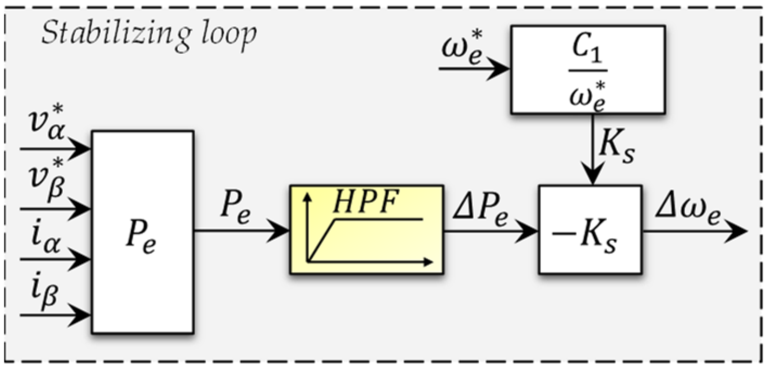

Figure 15. Block diagram of the stabilizing loop based on active power calculation.

4.2. Constant Power Factor Control Loop

The stable V/f control can be extended to maintain specific operational conditions. Such conditions can be satisfied by performing voltage amplitude correction with the additional loop. This paper proposes a novel constant power factor loop, where the power factor can be directly controlled in the voltage vector frame to the demanded value, as shown in Figure 16.

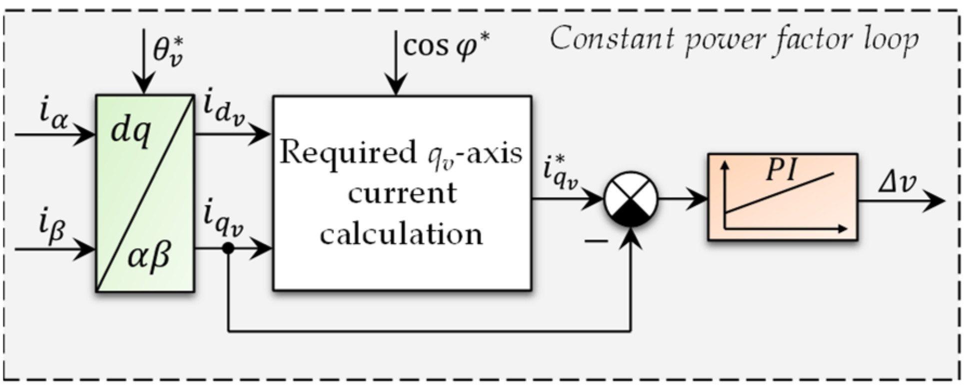

Figure 16. Block diagram of the constant power factor loop.

The constant power factor loop inputs are the measured $\alpha\beta$ currents transformed from the three-phase *abc* reference frame by employing Clarke transform as follows:

$$
\begin{aligned}
i_\alpha &= i_a \\
i_\beta &= \frac{\sqrt{3}}{3} i_b - \frac{\sqrt{3}}{3} i_c
\end{aligned}
\tag{37}
$$

The $\alpha\beta$ currents must be further transformed from the stationary $\alpha\beta$ frame to the new voltage vector frame $d_v q_v$, where the power factor can be controlled. The transformation to the $d_v q_v$ reference must be performed using Park transform with the required voltage vector position θ_v^*:

$$i_{d_v} = i_\alpha \cos(\theta_v^*) + i_\beta \sin(\theta_v^*) \tag{38}$$

$$i_{q_v} = -i_\alpha \sin(\theta_v^*) + i_\beta \cos(\theta_v^*) \tag{39}$$

In the new $d_v q_v$ reference frame, the d_v-axis is aligned with a stator voltage vector V_s as illustrated in Figure 17. The vector diagram in Figure 17a shows $d_v q_v$ currents in the voltage vector reference frame, where the power factor is controlled to $\cos\varphi < 1$. One of the other opportunities is to control the power factor to unity $\cos\varphi = 1$, as illustrated in Figure 17b. Then, the stator current vector I_s is aligned with the stator voltage vector V_s, and thus power factor angle φ becomes zero. It is evident from both figures that the power factor angle can be controlled by maintaining the q_v-axis current.

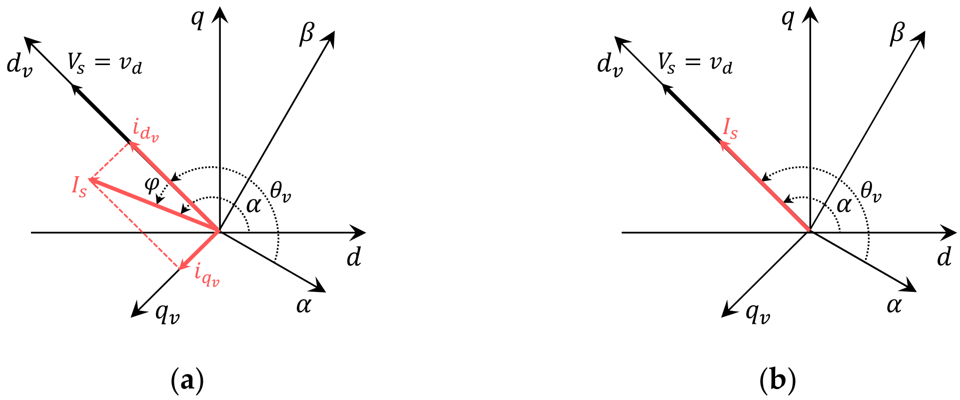

Figure 17. Vector diagram of PMSM: (**a**) $\varphi > 0$ ($\cos\varphi < 1$); (**b**) $\varphi = 0$ ($\cos\varphi = 1$).

The required q_v-axis current $i_{q_v}^*$ can be directly calculated with respect to the required power factor $\cos\varphi^*$ and the feedback $d_v q_v$ currents, as shown in Figure 18. Afterward, the PI controller forces the q_v-axis current from Park transform to the required value based on the demanded power factor. The output of the PI controller is the voltage amplitude correction Δv, which is sublimated from the required d-axis voltage v_d^*, while the required q-axis voltage v_q^* is maintained at zero. Therefore, the power factor can be directly controlled by adjusting the d-axis voltage amplitude.

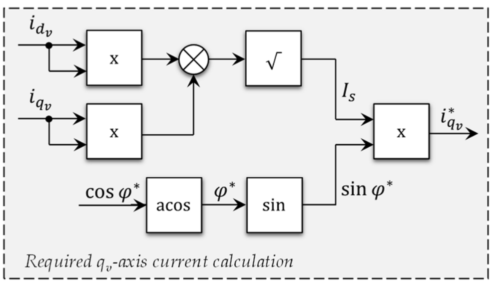

Figure 18. Required q_v-axis calculation block.

5. Experimental Results

In order to verify and compare the control performance of both sensorless approaches, a series of experiments have been carried out on the experimental setup described in Section 5.1.

5.1. Experimental Setup

The experiments were conducted on a power inverter module (PIM) with an apparent power of 150 kVA. The specifications of the PIM are available in Table A1 of Appendix A. DC power supplies were employed to ensure power for the PIM system basis chip (SBC) and the PIM DC bus. For the sensorless control algorithm's implementation and machine control, a microcontroller from the NXP Semiconductors, specifically MPC5775E, was used. The MPC5775E microcontrollers target automotive and industrial battery management and inverter applications. The communication between the microcontroller MPC5775E and PC was secured through the CAN interface. The application code was created in S32 Design Studio for Power Architecture. The USB Multilink Universal was utilized for debugging the application code from the PC to the target processor. FreeMASTER Run-Time Debugging tool observes the control variables and allows application users to control the machine current, speed, etc. A traction PMSM developed for golf cart applications with a rated power of 1.41 kW was used to determine experimental results. The parameters of the PMSM are provided in Table A2 of Appendix A. A DC dynamometer was used to provide load conditions for experimental PMSM. A torque sensor with a measuring range ±20 Nm was placed between the PMSM machine and DC dynamometer to provide accurate information about the actual motor torque. Photos of the experimental setup are shown in Figures 19 and 20.

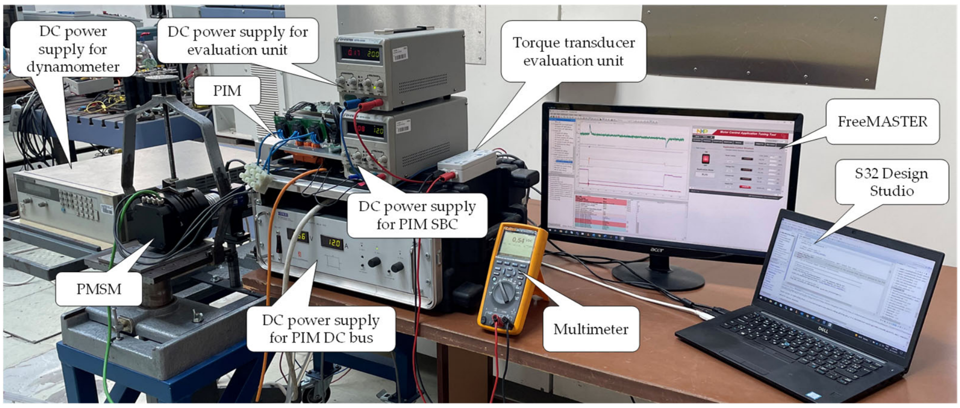

Figure 19. Experimental setup.

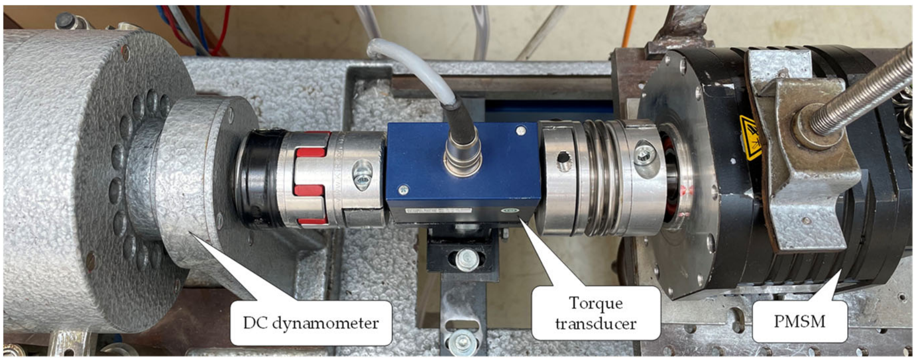

Figure 20. Experimental setup—enlarged view for PMSM, torque transducer, and DC dynamometer.

5.2. Experimental Verification of Stable V/f Control with CPF

In this section, a series of experiments for the V/f control with stabilization and CPF that were performed are described. The input parameters for this control strategy are presented in Table A3 of Appendix A. In Figure 21, the ramp-up to the nominal reference speed, change in speed direction, and 50% load applied at steady-state, with a required power factor of 1, is presented. The ramp was set up with a slope of 1000 rpm/s. The 50% load was applied from 8 s to 19 s in the forward direction and from 29 s to 40 s in the backward direction. The command to change the speed direction was set up at 21 s. The boost voltage of 3 V was applied to d-axis during motor start-up until 1000 rpm to overcome the starting issues. These issues are associated with a resistive voltage drop, which cannot be neglected at low speeds. Above the rotational speed n_r of 1000 rpm, the boost voltage is set back at 0 V, as is evident from the required d-axis voltage v_d^* in Figure 21.

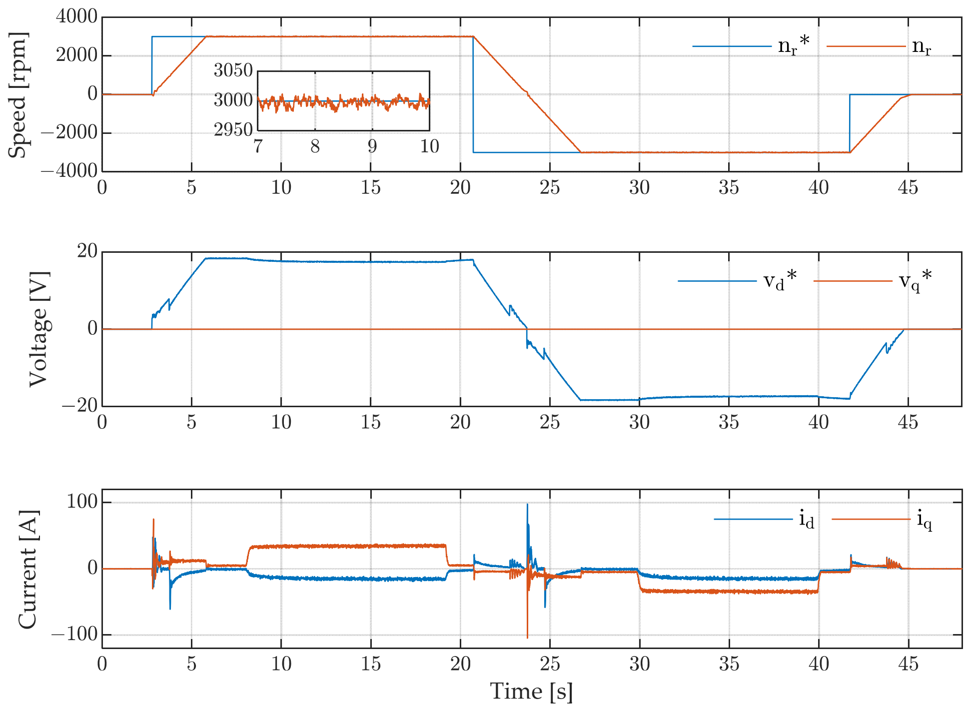

Figure 21. Ramp-up and ramp-down with the nominal reference speed and 50% load applied at steady-state, with a required power factor of 1: speed, dq voltages, dq currents.

In Figure 22, the same conditions were applied except for the applied load, which was increased to 75%.

In Figure 23, the applied load to the machine was increased to 100%. However, as evident from the figure, the machine cannot hold such a load, and the system becomes unstable. The reason behind the control failure lies in the required power factor. At the power factor is equal to unity, the required d-axis voltage v_d^* decreases with the higher loads, leading the system to an unstable region.

At the lower power factor, e.g., equal to 0.95, the V/f control can operate under full-load conditions, avoiding system instabilities. This is demonstrated in Figure 24, where the control performance under 100% load is presented.

The speed profiles with changes to nominal reference speed by 1000 rpm in both directions with no-load are shown in Figures 25 and 26. The first shows the speed profile for a power factor equal to 1, while the second one shows the profile for the lower power factor of 0.95, which was previously verified under full-load conditions. As can be seen from both figures, the real motor speed n_r follows the reference speed n_r^* and the accuracy at steady-state is spectacular. The main difference lies in the start-up current, which is approximately four times higher with a required power factor of 0.95, as evident in Figures 25 and 26.

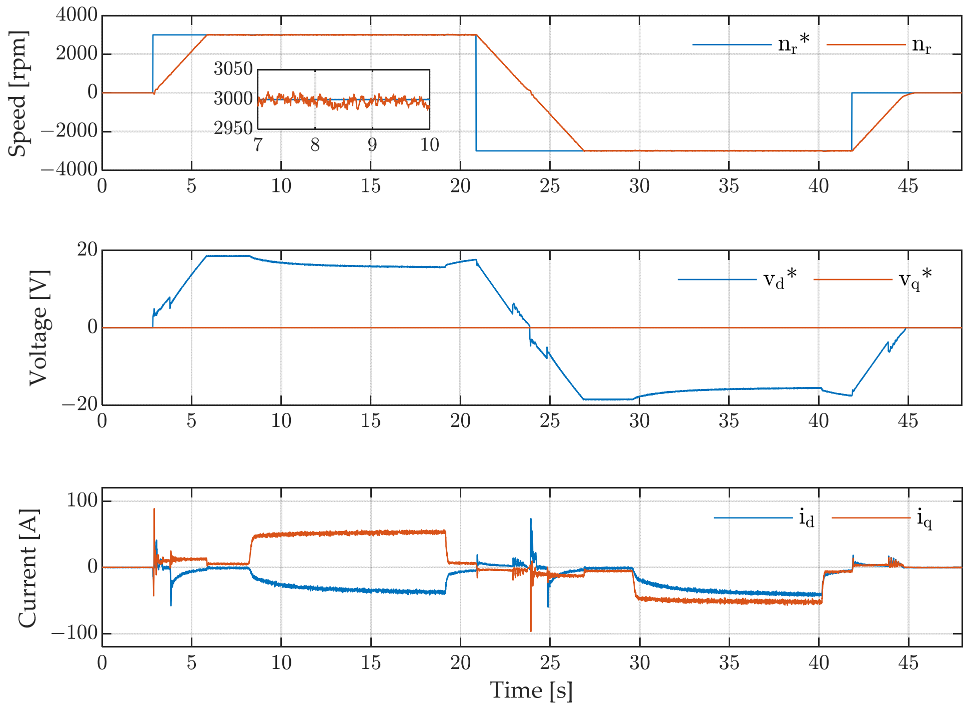

Figure 22. Ramp-up and ramp-down with the nominal reference speed and 75% load applied at steady-state, with a required power factor of 1: speed, *dq* voltages, *dq* currents.

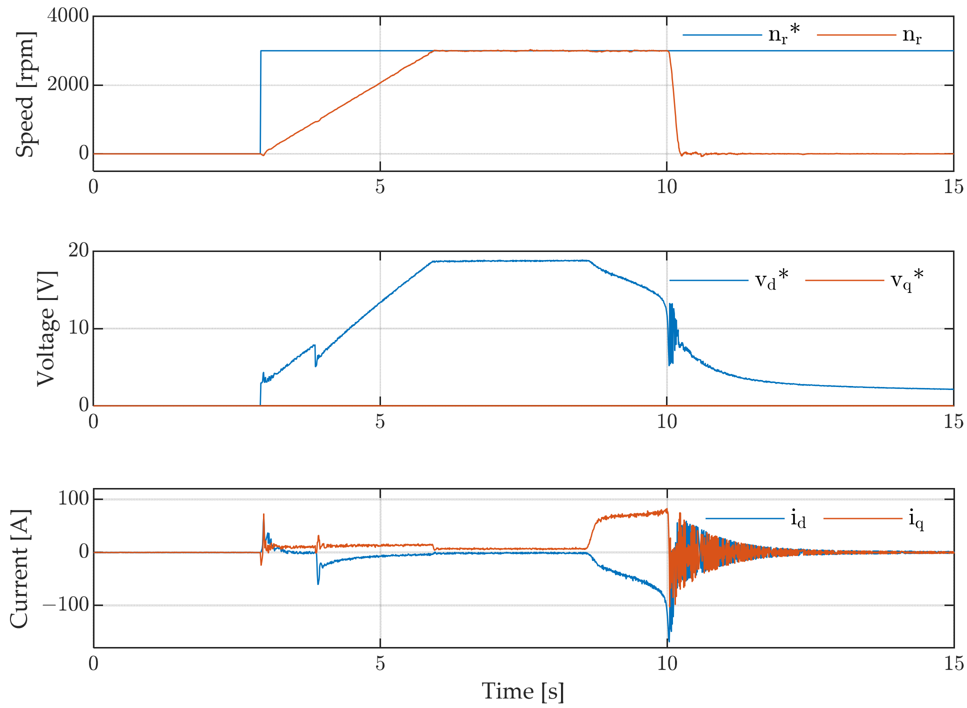

Figure 23. Ramp-up with the nominal reference speed and 100% load applied at steady-state, with a required power factor of 1: speed, *dq* voltages, *dq* currents.

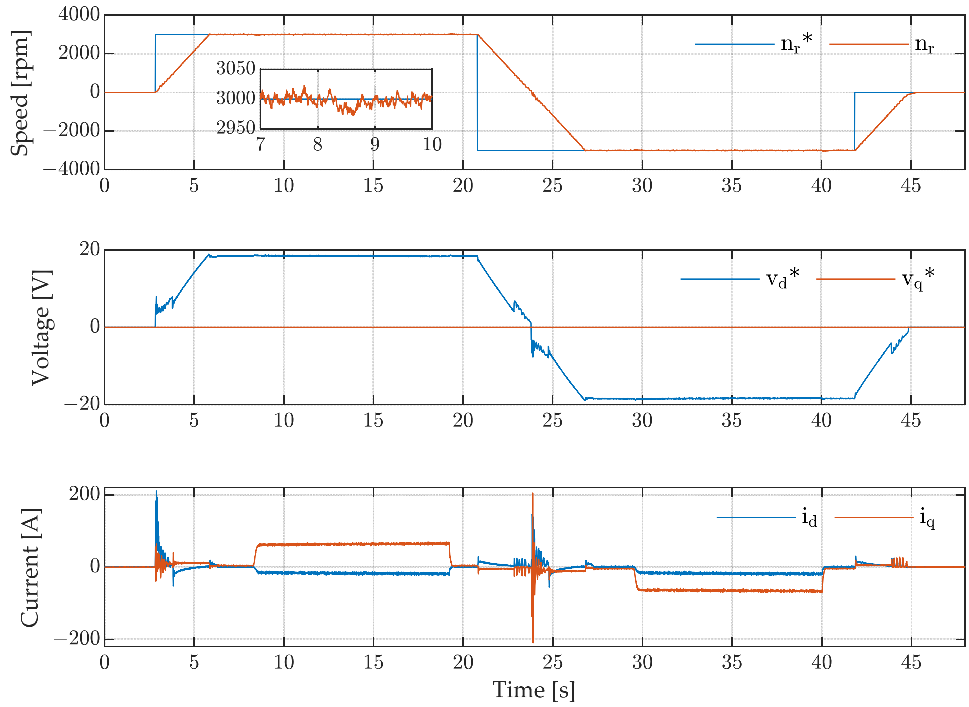

Figure 24. Ramp-up and ramp-down with the nominal reference speed and 100% load applied at steady-state, with a required power factor of 0.95: speed, *dq* voltages, *dq* currents.

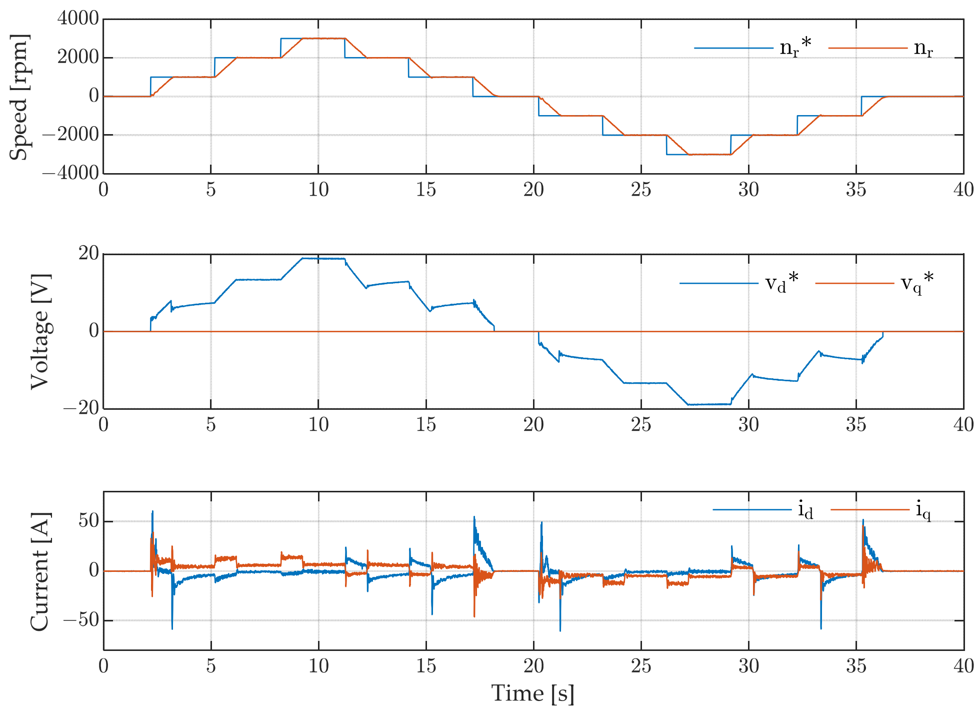

Figure 25. Speed profile up to nominal reference speed with no-load and required power factor of 1: speed, *dq* voltages, *dq* currents.

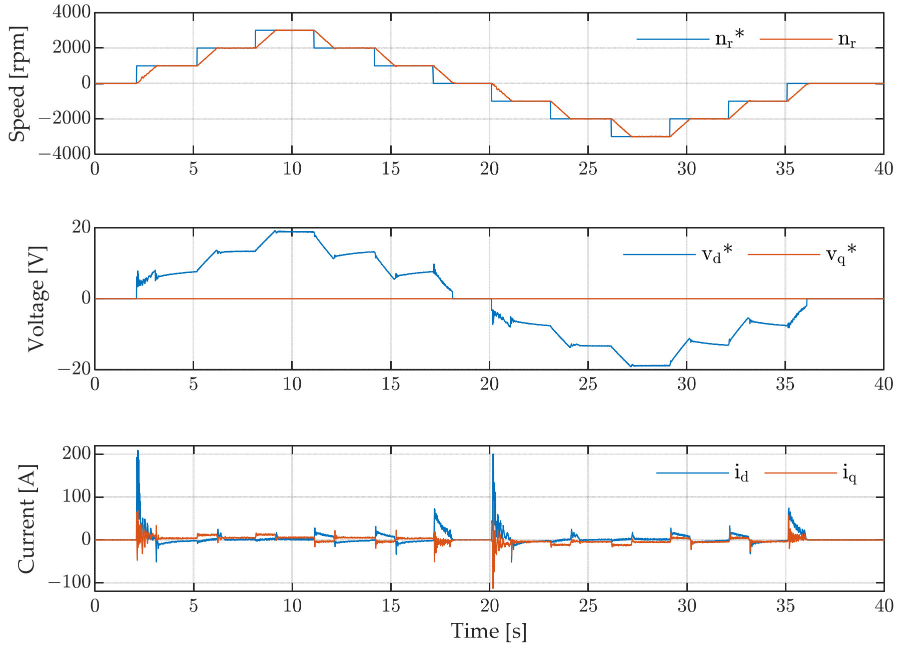

Figure 26. Speed profile up to nominal reference speed with no-load and required power factor of 0.95: speed, *dq* voltages, *dq* currents.

5.3. Experimental Verification of Luenberger-Type Back-EMF Observer in Sensorless FOC

In this section, similar experimental results are presented in order to compare the control performance of both sensorless techniques. The input parameters for the sensorless FOC are available in Table A4 of Appendix A. As stated in the Introduction, the model-based methods are not applicable at low speeds due to the unfavorable signal-to-noise ratio of the voltage measurements. Due to this disadvantage, stable V/f with CPF loop was used as a start-up control strategy for sensorless FOC. It uses a required d-axis voltage v_d^* to start-up the machine, while the required q-axis voltage v_q^* is maintained at zero. As evident in Figure 27, the motor start-up is smooth, without huge oscillations.

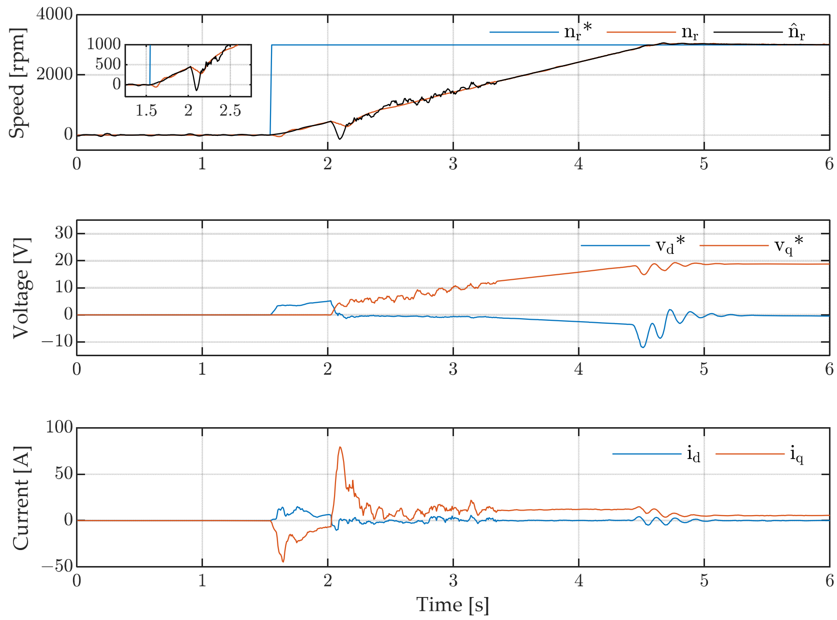

Figure 27. The motor start-up in stable V/f control with CPF and transition to the sensorless FOC with Luenberger-type back-EMF observer: speed, *dq* voltages, *dq* currents.

Transition to the sensorless FOC is applied at the rotational speed n_r of 500 rpm. Evaluation of low speed limit was discussed and verified in [25]. At the threshold speed, the estimated rotational speed $\hat{n}_r$ is set as a feedback value for the speed controller, as well as the estimated electrical position $\hat{\theta}_e$ to the Park transformations. During the transition between V/f and sensorless FOC, a small decrease in rotational speed n_r can be observed. The whole transition is considered to be a small disadvantage of such an approach. However, the decrease in the rotational speed n_r has not had a huge impact on the system stability and control performance of the sensorless method. After the transition, the d-axis current i_d is controlled to zero, while the q-axis current i_q provides the necessary torque to the machine.

In Figure 28, the ramp-up to the nominal reference speed of 3000 rpm, 50% load applied at steady-state, and change in speed direction is illustrated. The figure shows the robustness of the observer to the applied load disturbance and also a sufficient change in speed direction from the nominal speed of the machine 3000 rpm to −3000 rpm. At the lower speeds, sensorless FOC with Luenberger-type back-EMF observer was switched to the stable V/f control with CPF loop to provide adequate operation.

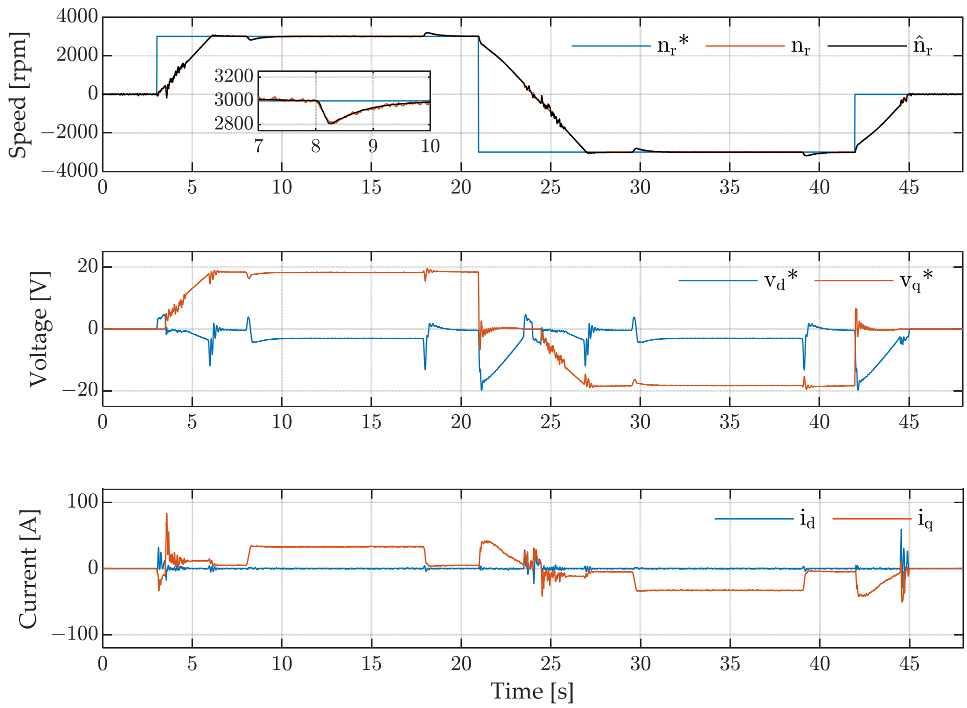

Figure 28. Ramp-up and ramp-down with the nominal reference speed and 50% load applied at steady-state: speed, *dq* voltages, *dq* currents.

Figure 29 shows a similar experimental verification. However, 75% load is applied to the machine. The experimental results show similar behavior and also robustness against such load disturbance.

Finally, in Figure 30, the applied load is increased to 100%, which corresponds to the nominal torque of the experimental PMSM machine. It is obvious that the sensorless FOC with Luenberger-type back-EMF observer is also operating properly under full-load machine conditions.

Compared to the same experimental procedure with stable V/f control in Figure 24, it is evident that stable V/f control with CPF has a better response to the load disturbance. In the sensorless FOC, the decrease in speed after the applied load is more significant.

Figure 31 shows the speed profile up to the nominal reference speed of 3000 rpm with no-load conditions.

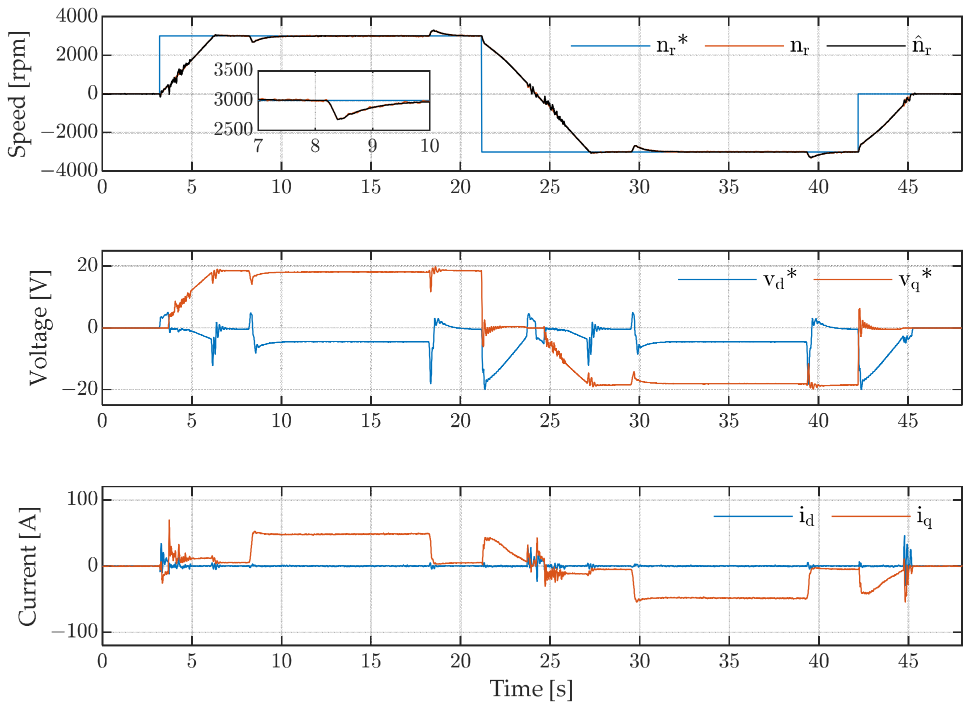

Figure 29. Ramp-up and ramp-down with the nominal reference speed and 75% load applied at steady-state: speed, *dq* voltages, *dq* currents.

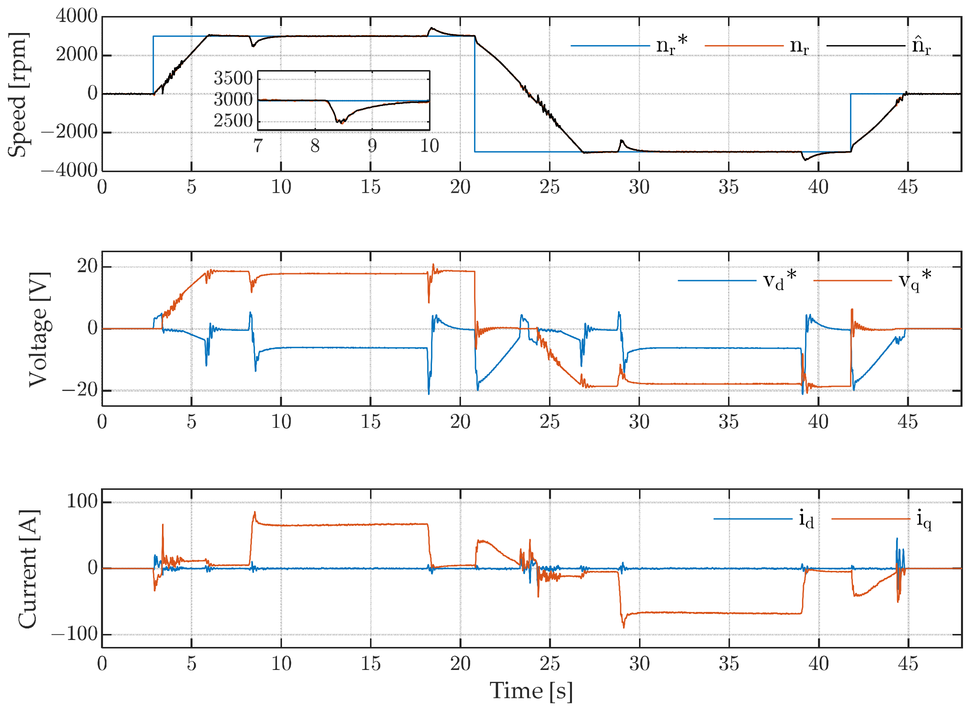

Figure 30. Ramp-up and ramp-down with the nominal reference speed and 100% load applied at steady-state: speed, *dq* voltages, *dq* currents.

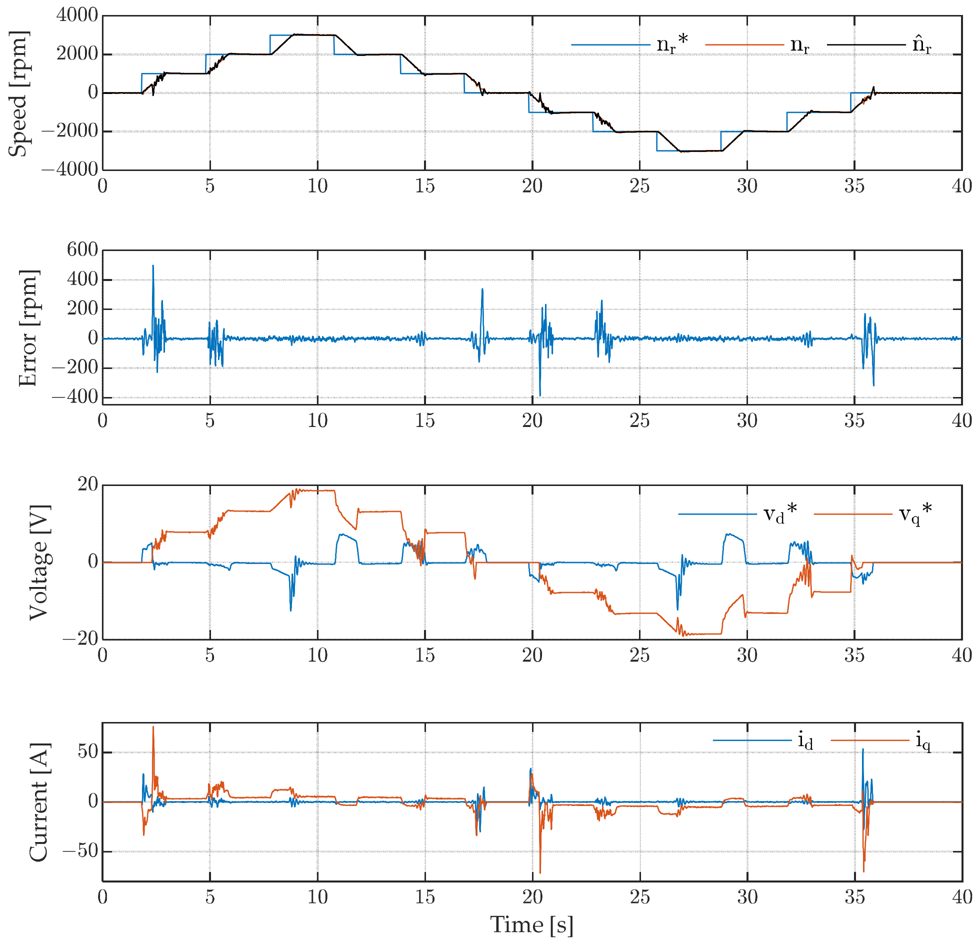

Figure 31. Speed profile up to nominal reference speed with no-load: speed, speed error, *dq* voltages, *dq* currents.

This figure can be used to determine the accuracy of the sensorless FOC with Luenberger-type back-EMF observer in a wide speed range. The result is that the estimated rotational speed is tracking the real motor speed with very high accuracy, which is evident from the speed error. Slight deviations are present in the motor transient due to switching between two methods during motor start-up. The other reason for the small oscillations lies in the controllers bandwidth.

5.4. Comparison of the Main Features for Stable V/f with CPF and Sensorless FOC with Luenberger-Type Back-EMF Observer

The comparison of the main features regarding control performance of both sensorless control strategies is presented in Table 3.

Some of the statements were verified experimentally within the article, e.g., accuracy, load disturbance response, start-up, and structure tuning.

The dynamics of both control structures are good. However, sensorless FOC could provide a faster speed response when increasing the bandwidth of the controllers. In the case of stable V/f control, the parameters of the stabilizing loop should be modified to improve the control dynamics.

Parameters dependence of the back-EMF observer was discussed in Section 3.2, while the stable V/f is completely independent of the machine parameters. This is considered as the biggest advantage, because the machine parameters change during motor operation, e.g., with saturation and temperature. Furthermore, these parameters are required for controller tuning in sensorless FOC, as derived in Sections 3.1.1 and 3.1.2.

Table 3. Comparison between stable V/f with CPF and sensorless FOC with Luenberger-type back-EMF observer.

Parameter	Stable *V*/*f* with CPF	Sensorless FOC with Luenberger-Type Back-EMF Observer
Accuracy	High	High
Dynamics	Good	Very good
Parameters dependence	Low	Medium
Computational time	Low	High
Load disturbance response	Very good	Good
Start-up	Good	-
Structure tuning	Easy	Hard
Low-speed operation	Bad	-

Computational time can be determined analytically based on the complexity of both sensorless control structures. Comparing Tables 1 and 2, it is evident that sensorless FOC is more complex and requires more computational time and high-performance MCU. Furthermore, the start-up control strategy has to be used regarding sensorless FOC, which further increases the complexity of the whole structure.

Structure tuning is more complex for sensorless FOC, where the gains of speed and current controllers have to be calculated. For the calculation, it is necessary to know the machine parameters, which have to be measured or obtained by the machine manufacturer. In stable V/f control, just a few parameters have to be set up properly, including stabilizing loop parameters and the controller gains in the CPF loop.

Low-speed operation is not acceptable for both sensorless control strategies. In the stable V/f control with CPF, boost voltage has to be applied in such a region to properly control the machine at low speeds. Sensorless FOC with Luenberger-type back-EMF observer cannot even be used in such a region due to the unfavorable signal-to-noise ratio of the voltage measurements, which is the main disadvantage of the back-EMF-based sensorless methods.

6. Conclusions

A novel CPF loop for stable V/f control of PMSM is proposed in this paper. The proposed sensorless control strategy is robust against machine parameters variation and offers a low-cost and simple-to-implement solution. It also allows controlling the motor power factor without dependence on machine parameters with the new CPF loop in the $d_v q_v$ reference frame. The main advantages of such a structure are speed control accuracy, parameter dependence, and computational time. The proposed control strategy was also compared against the traditional sensorless FOC with a Luenberger-type back-EMF observer within the paper. The back-EMF observer depends on the PMSM model, so it is necessary to know the machine parameters. The strategy with a back-EMF observer can be used just in the mid- and high-speed regions but with more than satisfactory control performance. However, due to the low-speed performance disadvantage, the stable V/f was also used as a start-up control strategy for sensorless FOC with the Luenberger-type back-EMF observer, providing satisfactory results. The experimental verification on a 1.41 kW PMSM machine designed for golf cart traction applications shows that stable V/f with a CPF loop seems to be more attractive than the back-EMF-based method regarding sensorless speed control.

Author Contributions: Conceptualization, M.V.; methodology, M.V. and P.M.; software, M.V. and L.G.; validation, M.V. and P.M.; formal analysis, M.V.; investigation, M.V.; resources, M.V.; data curation, M.V.; writing—original draft preparation, M.V.; writing—review and editing, L.G. and P.M.; visualization, M.V.; supervision, L.G. and P.M.; project administration, P.M.; funding acquisition, P.M. All authors have read and agreed to the published version of the manuscript.

Funding: This research was funded by the Slovak Scientific Grant Agency VEGA for project support 1/0795/21.

Institutional Review Board Statement: Not applicable.

Informed Consent Statement: Not applicable.

Data Availability Statement: Data sharing not applicable.

Conflicts of Interest: The authors declare no conflict of interest.

Appendix A

Table A1. Parameters of PIM.

Parameter	Symbol	Value	Unit
Apparent power	S_N	150	kVA
Nominal voltage	V_N	340	V
Peak current	I_{pk}	420	A
PWM switching frequency	f_{PWM}	3–12	kHz
Maximum electrical efficiency	η_{max}	98	%

Table A2. Parameters of PMSM.

Parameter	Symbol	Value	Unit
Rated power	P_N	1.41	kW
Rated speed	n_N	3000	rpm
Rated torque	T_N	4.5	Nm
Rated current	I_N	44.18	A
Rated frequency	f_N	250	Hz
Pole pairs	p	5	-
Stator resistance	R_s	0.011	Ω
d-axis inductance	L_d	0.052	mH
q-axis inductance	L_q	0.059	mH
Permanent magnet flux linkage	ψ_{pm}	0.0108	Wb
Motor inertia	J_m	5.39	kg·cm^2
System inertia	J_s	59.5	kg·cm^2

Table A3. Parameters for the Stable V/f control with CPF.

Parameter	Symbol	Value	Unit
Stabilizing loop constant	C_1	20	-
HPF time constant	τ_H	15.9	ms
Proportional gain of the PI controller in the CPF loop	K_{P_v}	0.05	-
Integral gain of the PI controller in the CPF loop	K_{I_v}	1×10^{-5}	-

Table A4. Parameters for the Sensorless FOC with Luenberger-type back-EMF observer.

Parameter	Symbol	Value	Unit
Natural frequency of the speed controller	f_{0_ω}	0.25	Hz
Natural frequency of the d-axis and q-axis current controller	$f_{0_{dq}}$	100	Hz
Natural frequency of the back-EMF observer	$f_{0_{bemf}}$	100	Hz
Natural frequency of the tracking observer	$f_{0_{to}}$	4	Hz

References

1. Bolognani, S.; Oboe, R.; Zigliotto, M. Sensorless Full-Digital PMSM Drive with EKF Estimation of Speed and Rotor Position. *IEEE Trans. Ind. Electron.* **1999**, *46*, 184–191. [CrossRef]
2. Wang, Z.; Zheng, Y.; Zou, Z.; Cheng, M. Position Sensorless Control of Interleaved CSI Fed PMSM Drive with Extended Kalman Filter. *IEEE Trans. Magn.* **2012**, *48*, 3688–3691. [CrossRef]
3. Quang, N.K.; Hieu, N.T.; Ha, Q.P. FPGA-Based Sensorless PMSM Speed Control Using Reduced-Order Extended Kalman Filters. *IEEE Trans. Ind. Electron.* **2014**, *61*, 6574–6582. [CrossRef]
4. Orlowska-Kowalska, T.; Dybkowski, M. Stator-Current-Based MRAS Estimator for a Wide Range Speed-Sensorless Induction-Motor Drive. *IEEE Trans. Ind. Electron.* **2010**, *57*, 1296–1308. [CrossRef]
5. Zhu, Y.; Tao, B.; Xiao, M.; Yang, G.; Zhang, X.; Lu, K. Luenberger Position Observer Based on Deadbeat-Current Predictive Control for Sensorless PMSM. *Electronics* **2020**, *9*, 1325. [CrossRef]
6. Chi, S.; Zhang, Z.; Xu, L. Sliding-Mode Sensorless Control of Direct-Drive PM Synchronous Motors for Washing Machine Applications. *IEEE Trans. Ind. Appl.* **2009**, *45*, 582–590. [CrossRef]
7. Kim, H.; Son, J.; Lee, J. A High-Speed Sliding-Mode Observer for the Sensorless Speed Control of a PMSM. *IEEE Trans. Ind. Electron.* **2011**, *58*, 4069–4077. [CrossRef]
8. Rivera Dominguez, J.; Navarrete, A.; Meza, M.A.; Loukianov, A.G.; Canedo, J. Digital Sliding-Mode Sensorless Control for Surface-Mounted PMSM. *IEEE Trans. Ind. Inform.* **2014**, *10*, 137–151. [CrossRef]
9. Song, X.; Fang, J.; Han, B.; Zheng, S. Adaptive Compensation Method for High-Speed Surface PMSM Sensorless Drives of EMF-Based Position Estimation Error. *IEEE Trans. Power Electron.* **2016**, *31*, 1438–1449. [CrossRef]
10. Liang, D.; Li, J.; Qu, R. Sensorless Control of Permanent Magnet Synchronous Machine Based on Second-Order Sliding-Mode Observer with Online Resistance Estimation. *IEEE Trans. Ind. Appl.* **2017**, *53*, 3672–3682. [CrossRef]
11. Wang, Y.; Xu, Y.; Zou, J. Sliding-Mode Sensorless Control of PMSM with Inverter Nonlinearity Compensation. *IEEE Trans. Power Electron.* **2019**, *34*, 10206–10220. [CrossRef]
12. Morimoto, S.; Kawamoto, K.; Sanada, M.; Takeda, Y. Sensorless Control Strategy for Salient-Pole PMSM Based on Extended EMF in Rotating Reference Frame. *IEEE Trans. Ind. Appl.* **2002**, *38*, 1054–1061. [CrossRef]
13. Zhiqian, C.; Tomita, M.; Doki, S.; Okuma, S. An Extended Electromotive Force Model for Sensorless Control of Interior Permanent-Magnet Synchronous Motors. *IEEE Trans. Ind. Electron.* **2003**, *50*, 288–295. [CrossRef]
14. Burgos, R.; Kshirsagar, P.; Lidozzi, A.; Wang, F.; Boroyevich, D. Mathematical Model and Control Design for Sensorless Vector Control of Permanent Magnet Synchronous Machines. In Proceedings of the 2006 IEEE Workshops on Computers in Power Electronics, New York, NY, USA, 16–19 July 2006; pp. 76–82.
15. Kshirsagar, P.; Burgos, R.P.; Jang, J.; Lidozzi, A.; Wang, F.; Boroyevich, D.; Sul, S.-K. Implementation and Sensorless Vector-Control Design and Tuning Strategy for SMPM Machines in Fan-Type Applications. *IEEE Trans. Ind. Appl.* **2012**, *48*, 2402–2413. [CrossRef]
16. Piippo, A.; Hinkkanen, M.; Luomi, J. Analysis of an Adaptive Observer for Sensorless Control of Interior Permanent Magnet Synchronous Motors. *IEEE Trans. Ind. Electron.* **2008**, *55*, 570–576. [CrossRef]
17. Fatu, M.; Teodorescu, R.; Boldea, I.; Andreescu, G.-D.; Blaabjerg, F. I-F Starting Method with Smooth Transition to EMF Based Motion-Sensorless Vector Control of PM Synchronous Motor/Generator. In Proceedings of the 2008 IEEE Power Electronics Specialists Conference, Rhodes, Greece, 15–19 June 2008; pp. 1481–1487.
18. Wang, Z.; Lu, K.; Blaabjerg, F. A Simple Startup Strategy Based on Current Regulation for Back-EMF-Based Sensorless Control of PMSM. *IEEE Trans. Power Electron.* **2012**, *27*, 3817–3825. [CrossRef]
19. Wang, M.; Xu, Y.; Zou, J.; Lan, H. An Optimized I-F Startup Method for BEMF-Based Sensorless Control of SPMSM. In Proceedings of the 2017 IEEE Transportation Electrification Conference and Expo, Asia-Pacific (ITEC Asia-Pacific), Harbin, China, 7–10 August 2017; pp. 1–6.
20. Inoue, Y.; Yamada, K.; Morimoto, S.; Sanada, M. Effectiveness of Voltage Error Compensation and Parameter Identification for Model-Based Sensorless Control of IPMSM. *IEEE Trans. Ind. Appl.* **2009**, *45*, 213–221. [CrossRef]
21. Ichikawa, S.; Tomita, M.; Doki, S.; Okuma, S. Sensorless Control of Synchronous Reluctance Motors Based on Extended EMF Models Considering Magnetic Saturation with Online Parameter Identification. *IEEE Trans. Ind. Appl.* **2006**, *42*, 1264–1274. [CrossRef]
22. Yoo, J.; Lee, Y.; Sul, S.-K. Back-EMF Based Sensorless Control of IPMSM with Enhanced Torque Accuracy Against Parameter Variation. In Proceedings of the 2018 IEEE Energy Conversion Congress and Exposition (ECCE), Portland, OR, USA, 23–27 September 2018; pp. 3463–3469.
23. Hejny, R.W.; Lorenz, R.D. Evaluating the Practical Low-Speed Limits for Back-EMF Tracking-Based Sensorless Speed Control Using Drive Stiffness as a Key Metric. *IEEE Trans. Ind. Appl.* **2011**, *47*, 1337–1343. [CrossRef]
24. Inoue, Y.; Kawaguchi, Y.; Morimoto, S.; Sanada, M. Performance Improvement of Sensorless IPMSM Drives in a Low-Speed Region Using Online Parameter Identification. *IEEE Trans. Ind. Appl.* **2011**, *47*, 798–804. [CrossRef]
25. Zossak, S.; Sovicka, P.; Sumega, M.; Rafajdus, P. Evaluating Low Speed Limit of Back-EMF Observer for Permanent Magnet Synchronous Motor. *Transp. Res. Procedia* **2019**, *40*, 610–615. [CrossRef]
26. Corley, M.J.; Lorenz, R.D. Rotor Position and Velocity Estimation for a Salient-Pole Permanent Magnet Synchronous Machine at Standstill and High Speeds. *IEEE Trans. Ind. Appl.* **1998**, *34*, 784–789. [CrossRef]

27. Jung-Ik, H.; Ide, K.; Sawa, T.; Sul, S.-K. Sensorless Rotor Position Estimation of an Interior Permanent-Magnet Motor from Initial States. *IEEE Trans. Ind. Appl.* **2003**, *39*, 761–767. [CrossRef]
28. Xie, G.; Lu, K.; Dwivedi, S.K.; Rosholm, J.R.; Blaabjerg, F. Minimum-Voltage Vector Injection Method for Sensorless Control of PMSM for Low-Speed Operations. *IEEE Trans. Power Electron.* **2016**, *31*, 1785–1794. [CrossRef]
29. Kim, S.-I.; Im, J.-H.; Song, E.-Y.; Kim, R.-Y. A New Rotor Position Estimation Method of IPMSM Using All-Pass Filter on High-Frequency Rotating Voltage Signal Injection. *IEEE Trans. Ind. Electron.* **2016**, *63*, 6499–6509. [CrossRef]
30. Ji-Hoon, J.; Sul, S.-K.; Jung-Ik, H.; Ide, K.; Sawamura, M. Sensorless Drive of Surface-Mounted Permanent-Magnet Motor by High-Frequency Signal Injection Based on Magnetic Saliency. *IEEE Trans. Ind. Appl.* **2003**, *39*, 1031–1039. [CrossRef]
31. Shih-Chin, Y.; Lorenz, R.D. Surface Permanent Magnet Synchronous Machine Position Estimation at Low Speed Using Eddy-Current-Reflected Asymmetric Resistance. *IEEE Trans. Power Electron.* **2012**, *27*, 2595–2604. [CrossRef]
32. Yang, S.-C.; Lorenz, R.D. Surface Permanent-Magnet Machine Self-Sensing at Zero and Low Speeds Using Improved Observer for Position, Velocity, and Disturbance Torque Estimation. *IEEE Trans. Ind. Appl.* **2012**, *48*, 151–160. [CrossRef]
33. Seilmeier, M.; Piepenbreier, B. Sensorless Control of PMSM for the Whole Speed Range Using Two-Degree-of-Freedom Current Control and HF Test Current Injection for Low-Speed Range. *IEEE Trans. Power Electron.* **2015**, *30*, 4394–4403. [CrossRef]
34. Young-Doo, Y.; Seung-Ki, S.; Morimoto, S.; Ide, K. High-Bandwidth Sensorless Algorithm for AC Machines Based on Square-Wave-Type Voltage Injection. *IEEE Trans. Ind. Appl.* **2011**, *47*, 1361–1370. [CrossRef]
35. Kim, D.; Kwon, Y.-C.; Sul, S.-K.; Kim, J.-H.; Yu, R.-S. Suppression of Injection Voltage Disturbance for High-Frequency Square-Wave Injection Sensorless Drive with Regulation of Induced High-Frequency Current Ripple. *IEEE Trans. Ind. Appl.* **2016**, *52*, 302–312. [CrossRef]
36. Xu, P.L.; Zhu, Z.Q. Novel Square-Wave Signal Injection Method Using Zero-Sequence Voltage for Sensorless Control of PMSM Drives. *IEEE Trans. Ind. Electron.* **2016**, *63*, 7444–7454. [CrossRef]
37. Ni, R.; Xu, D.; Blaabjerg, F.; Lu, K.; Wang, G.; Zhang, G. Square-Wave Voltage Injection Algorithm for PMSM Position Sensorless Control with High Robustness to Voltage Errors. *IEEE Trans. Power Electron.* **2017**, *32*, 5425–5437. [CrossRef]
38. Wang, G.; Valla, M.; Solsona, J. Position Sensorless Permanent Magnet Synchronous Machine Drives—A Review. *IEEE Trans. Ind. Electron.* **2020**, *67*, 5830–5842. [CrossRef]
39. Hong, J.; Jung, S.; Nam, K. An Incorporation Method of Sensorless Algorithms: Signal Injection and Back EMF Based Methods. In Proceedings of the 2010 International Power Electronics Conference—ECCE ASIA, Sapporo, Japan, 21–24 June 2010; pp. 2743–2747.
40. Yang, S.-C.; Hsu, Y.-L. Full Speed Region Sensorless Drive of Permanent-Magnet Machine Combining Saliency-Based and Back-EMF-Based Drive. *IEEE Trans. Ind. Electron.* **2017**, *64*, 1092–1101. [CrossRef]
41. Bose, B.K. Control and Estimation of Induction Motor Drives. In *Modern Power Electronics and AC Drives*; Pearson Education Inc.: Upper Saddle River, NJ, USA, 2002; p. 339.
42. Perera, P.D.C. Mathematical Models and Control Properties. In *Sensorless Control of Permanent-Magnet Synchronous Motor Drives*; Aalborg University: Aalborg, Denmark, 2002.
43. Perera, P.D.C.; Blaabjerg, F.; Pedersen, J.K.; Thogersen, P. A Sensorless, Stable V/f Control Method for Permanent-Magnet Synchronous Motor Drives. *IEEE Trans. Ind. Appl.* **2003**, *39*, 783–791. [CrossRef]
44. Itoh, J.-I.; Nomura, N.; Ohsawa, H. A Comparison between V/f Control and Position-Sensorless Vector Control for the Permanent Magnet Synchronous Motor. In Proceedings of the Power Conversion Conference-Osaka 2002 (Cat. No.02TH8579), Osaka, Japan, 2–5 April 2002; pp. 1310–1315.
45. Kiuchi, M.; Ohnishi, T.; Hagiwara, H.; Yasuda, Y. V/f Control of Permanent Magnet Synchronous Motors Suitable for Home Appliances by DC-Link Peak Current Control Method. In Proceedings of the 2010 International Power Electronics Conference—ECCE ASIA, Sapporo, Japan, 21–24 June 2010; pp. 567–573.
46. Sue, S.-M.; Hung, T.-W.; Liaw, J.-H.; Li, Y.-F.; Sun, C.-Y. A New MTPA Control Strategy for Sensorless V/f Controlled PMSM Drives. In Proceedings of the 2011 6th IEEE Conference on Industrial Electronics and Applications, Beijing, China, 21–23 June 2011; pp. 1840–1844.
47. Kim, W.-J.; Kim, S.-H. A Sensorless V/f Control Technique Based on MTPA Operation for PMSMs. In Proceedings of the 2018 IEEE Energy Conversion Congress and Exposition (ECCE), Portland, OR, USA, 23–27 September 2018; pp. 1716–1721.
48. Andreescu, G.-D.; Coman, C.-E.; Moldovan, A.; Boldea, I. Stable V/f Control System with Unity Power Factor for PMSM Drives. In Proceedings of the 2012 13th International Conference on Optimization of Electrical and Electronic Equipment (OPTIM), Brasov, Romania, 24–26 May 2012; pp. 432–438.
49. Coman, C.-E.; Agarlita, S.-C.; Andreescu, G.-D. V/f Control Strategy with Constant Power Factor for SPMSM Drives, with Experiments. In Proceedings of the 2013 IEEE 8th International Symposium on Applied Computational Intelligence and Informatics (SACI), Timisoara, Romania, 23–25 May 2013; pp. 147–151.
50. Agarlita, S.; Coman, C.; Andreescu, G.; Boldea, I. Stable V/f Control System with Controlled Power Factor Angle for Permanent Magnet Synchronous Motor Drives. *IET Electr. Power Appl.* **2013**, *7*, 278–286. [CrossRef]
51. Isfanuti, A.; Paicu, M.-C.; Andreescu, G.-D.; Tutelea, L.N.; Staudt, T.; Boldea, I. V/f with Stabilizing Loops and MTPA versus Sensorless FOC for PMSM Drives. *Electr. Power Compon. Syst.* **2020**, *48*, 1197–1210. [CrossRef]

52. Vidlak, M.; Gorel, L.; Makys, P. Performance Evaluation, Analysis, and Comparison of the Back-EMF-Based Sensorless FOC and Stable V/f Control for PMSM. In Proceedings of the 2022 International Symposium on Power Electronics, Electrical Drives, Automation and Motion (SPEEDAM), Sorrento, Italy, 22 June 2022; pp. 318–323.
53. Consoli, A.; Scelba, G.; Scarcella, G.; Cacciato, M. An Effective Energy-Saving Scalar Control for Industrial IPMSM Drives. *IEEE Trans. Ind. Electron.* **2013**, *60*, 3658–3669. [CrossRef]
54. Lee, K.; Han, Y. MTPA Control Strategy Based on Signal Injection for V/f Scalar-Controlled Surface Permanent Magnet Synchronous Machine Drives. *IEEE Access* **2020**, *8*, 96036–96044. [CrossRef]
55. Hrabovcová, V.; Rafajdus, P.; Makyš, P. *Analysis of Electrical Machines*; IntechOpen: London, UK, 2020; ISBN 978-1-83880-207-3.
56. Vidlak, M.; Gorel, L.; Makys, P.; Stano, M. Sensorless Speed Control of Brushed DC Motor Based at New Current Ripple Component Signal Processing. *Energies* **2021**, *14*, 5359. [CrossRef]
57. Filka, R.; Balazovic, P.; Dobrucky, B. Transducerless Speed Control with Initial Position Detection for Low Cost PMSM Drives. In Proceedings of the 2008 13th International Power Electronics and Motion Control Conference, Poznan, Poland, 1–3 September 2008; pp. 1402–1408.